Composite Mesoscale Environmental Conditions Influencing Tornado Frequencies in Landfalling Tropical Cyclones

STANLEY B. TRIER,[a] DAVID A. AHIJEVYCH,[a] DEREKA CARROLL-SMITH,[a,b] GEORGE H. BRYAN,[a] AND ROGER EDWARDS[c]

[a] *National Center for Atmospheric Research, Boulder, Colorado*
[b] *Jackson State University, Jackson, Mississippi*
[c] *NOAA/Storm Prediction Center, Norman, Oklahoma*

(Manuscript received 26 December 2022, in final form 26 August 2023, accepted 9 October 2023)

ABSTRACT: Spatial patterns of tropical cyclone tornadoes (TCTs), and their relationship to patterns of mesoscale predictors within U.S. landfalling tropical cyclones (LTCs) are investigated using multicase composites from 27 years of reanalysis data (1995–2021). For 72 cases of LTCs with wide-ranging TC intensities at landfall, daytime TCT frequency maxima are found in the northeast, right-front, and downshear-right quadrants when their composites are constructed in ground-relative, TC-heading relative, and environmental shear relative coordinates, respectively. TCT maxima are located near maxima of 10-m–700-hPa bulk wind difference (BWD), which are enhanced by the TC circulation. This proxy for bulk vertical shear in roughly the lowest 3 km is among the best predictors of maximum TCT frequency. Relative to other times, the position of maximum TCT frequency during the afternoon shifts ~100 km outward from the LTC center toward larger MLCAPE values. Composites containing the strongest LTCs have the strongest maximum 10-m–700-hPa and 10-m–500-hPa BWDs (~20 m s^{-1}) with nearby maximum frequencies of TCTs. Corresponding composites containing weaker LTCs but still many TCTs, had bulk vertical shear values that were ~20% smaller (~16 m s^{-1}). Additional composites of cases having similarly weak average LTC strength at landfall, but few or no TCTs, had both maximum bulk vertical shears that were an additional ~20% lower (~12 m s^{-1}) and smaller MLCAPE. TCT environments occurring well inland are distinguished from others by having stronger westerly shear and a west–east-oriented baroclinic zone (i.e., north–south temperature gradient) that enhances mesoscale ascent and deep convection on the LTC's east side.

KEYWORDS: Tornadoes; Tropical cyclones; Mesoscale processes

1. Introduction

Landfalling tropical cyclones (LTCs) constitute a major threat to the southeastern United States. Among their numerous associated hazards are widespread wind damage and storm surge within coastal zones, and torrential rains and tornadoes which can occur both near the coast and much farther inland. Tropical cyclone tornadoes (TCTs) are common within tropical cyclone rainbands and account for approximately 3% of the fatalities associated with Atlantic tropical cyclones (Rappaport 2014). In the current study we use model reanalysis fields to clarify environmental conditions of tornadic and nontornadic LTC cases by producing composites (multicase averages) for different objectively defined TCT environment types.

Climatological studies (e.g., McCaul 1991; Schultz and Cecil 2009), and a comprehensive review (Edwards 2012) indicate that TCTs are typically much weaker than their Great Plains counterparts, owing largely to reduced CAPE in their environments. However, idealized modeling studies with initial thermodynamic and wind profiles representing TCT environments (e.g., McCaul and Weisman 1996, 2001; McCaul and Cohen 2002) suggest a similar supercell dynamical character of the parent thunderstorms responsible for producing TCTs in LTC outer rainbands. This similarity has been attributed in both observations (e.g., Novlan and Gray 1974) and the idealized modeling studies to strong lower-tropospheric (e.g., 0–3 km AGL, AGL omitted hereafter) vertical shear comparable to or even stronger than that found in Great Plains supercell environments. The supercell storms in LTC outer rainbands are typically smaller and shallower than in the Great Plains, which has been confirmed by observational studies (e.g., Spratt et al. 1997; Eastin and Link 2009; Baker et al. 2009). Supercell storms in LTC outer rainbands have also been recently simulated using modeling frameworks (e.g., Mashiko et al. 2009; Morin and Parker 2011) that are more realistic than those of the earlier initially horizontally homogeneous idealized studies.

Both the McCaul (1991) and Schultz and Cecil (2009) climatologies found a significant diurnal cycle of TCTs, with greater occurrence during the daytime hours. Morin and Parker (2011) found in their simulations that simulated supercells were more numerous, intense, and long-lived when TC landfalls occurred during the day. A likely explanation proposed in many previous studies concerns effects of thermodynamic destabilization resulting from surface heating. The increase of TCTs with increasing distance from the TC center during the day (Edwards 2012) suggests that thermodynamic destabilization and other possible effects influencing TCT production are not uniform across LTC circulations.

TCTs are most common within 12–24 h of TC landfall (Schultz and Cecil 2009). However, there are many exceptions and TC-related tornado outbreaks can occur up to several days after TC landfall (Nowotarski et al. 2021) and at distances

Corresponding author: Stanley B. Trier, trier@ucar.edu

DOI: 10.1175/WAF-D-22-0227.1

TABLE 1. Case numbers (second column), total number of postlandfall TCTs during the LTC lifetime (third column), number of TCTs in the most tornadic diurnal cycle after TCT landfall (fourth column), numbers of weak (fifth column) and strong (sixth column) TCTs during the most tornadic postlandfall diurnal cycle, and number of TCTs from 1330 to 0129 UTC (seventh column), and 0130–1329 UTC (eighth column) during this diurnal cycle for composite TCT environment type categories (first column). Parenthetical entries in each column indicate the average number of TCTs per case.

TCT environment type	Cases	TCT total	24-h TCTs	EF0–1	≥EF2	Day TCTs	Night TCTs
STRONG LTC–MANY TCTs	16	799 (50)	358 (22)	330 (21)	28 (2)	278 (17)	80 (5)
WEAK LTC–MANY TCTs	23	481 (21)	277 (12)	257 (11)	20 (1)	188 (8)	89 (4)
SOME TCTs	13	76 (6)	49 (4)	48 (4)	1 (0)	28 (2)	21 (2)
FEW OR NO TCTs	20	19 (1)	18 (1)	17 (1)	1 (0)	12 (1)	6 (0)
ALL–CASES	72	1375 (19)	702 (10)	652 (9)	50 (1)	506 (7)	196 (3)

of many hundreds of kilometers from the coast (e.g., Edwards et al. 2012). The tendency for TCTs to occur most often in the LTC right-front (relative to TC motion) or northeast quadrant, is a long recognized climatological attribute (e.g., Hill et al. 1966; Novlan and Gray 1974; Gentry 1983; McCaul 1991) and is hypothesized to result primarily from vertical shear enhancements in this region. The LTC may encounter stronger environmental westerlies when it moves farther inland and northward, which may contribute to vertical shear enhancements (McCaul 1991; Verbout et al. 2007; Moore and Dixon 2015). Schenkel et al. (2021) found that inland TCT environments possessed particularly strong environmental vertical shear through the LTC's approximate depth.

Though tornadoes are much more common in strong LTCs (Edwards 2012), weak LTCs can also produce numerous tornadoes. Therefore, forecasters need to be able to assess differences in environmental conditions between weak LTCs that produce many tornadoes and those that produce few or none, which is one objective of the current study. Examining predictor fields from model 3-hourly reanalyses together with TCT frequency data can provide greater detail on the spatial structure of TCT environmental predictors than previous studies that have relied primarily on twice-daily soundings. In the current study, our use of composites from reanalysis data for a wide variety of different TCT environment types, which include variations in LTC strength at landfall, extends past efforts (e.g., McCaul 1991; Eastin et al. 2014; Schenkel et al. 2020, 2021) to diagnose spatial patterns of TCT predictors within LTCs. We also use the composites to analyze the diurnal cycle of TCT environments, to highlight unique aspects of inland TCT environments, and to show how TC strength at landfall influences TCT production.

In section 2 we describe our data sources, different classes of composite TCT environments, and discuss our methodology used in producing the composites. Section 3 describes general aspects of the diurnal cycle of TCT environments. In section 4 we examine effects of TC landfall on TCT environments and assess the utility of different TCT environmental predictors. Section 5 contrasts TCT environments occurring at inland locations with other TCT environments.

2. Data and composites

The U.S. Atlantic LTC cases during the 27-yr period of 1995–2021 were identified from examination of the NOAA National Hurricane Center (NHC) archive. The timing, intensities, and positions relative to LTC centers of associated TCTs were determined using the tropical cyclone tornado (TCTOR) database (Edwards 2010; Edwards and Mosier 2022). These data were subsequently stratified based on different objectively defined TCT environment types (section 2a), and composites of environmental conditions for these different types were constructed using North American Regional Reanalysis (NARR) output (Mesinger et al. 2006) and additional TCT predictor fields derived from the NARR (section 2b).

a. LTC cases used for TCT environment composites

These TCT environment types for which environmental composites were produced are based on LTC intensity at landfall and the number of subsequent TCTs and include 1) strong LTCs that were classified as category-2 or greater hurricanes ($\|\mathbf{v}\|_{\max} \geq 83$ kt or 43.3 m s^{-1}) at landfall, and had many (i.e., ≥10) subsequent TCTs (hereafter STRONG LTC–MANY TCTs); 2) weak-to-intermediate intensity LTCs classified as either category-1 hurricanes (64 kt $\leq \|\mathbf{v}\|_{\max} \leq$ 82 kt or 32.7–43.2 m s^{-1}) or tropical storms (34 kt $\leq \|\mathbf{v}\|_{\max} \leq$ 63 kt or 17.4–32.6 m s^{-1}) at landfall, and similarly had ≥10 subsequent TCTs (hereafter WEAK LTC–MANY TCTs); 3) LTC cases of any intensity having 3–9 TCTs during their lifetimes (hereafter SOME TCTs); and 4) LTC cases of any intensity having ≤2 TCTs during their lifetimes (hereafter FEW OR NO TCTs).

Among the individual TCT environment types, STRONG LTC–MANY TCTs had the greatest average number of TCTs per case of 50 (Table 1, third column parentheses) for the 16 cases included in this composite, and relatively few LTCs in the 27-yr dataset having an intensity ≥ category 2 at landfall failed to produce the 10 or more TCTs during their lifetime required to meet this classification. However, there was much greater variability in TCT production among the overall LTC population, which motivated constructions of the WEAK LTC–MANY TCTs and FEW OR NO TCTs composites that together aim to better determine environmental factors supporting TCTs in weaker than average LTC circulations. The SOME TCTs composite had environmental conditions that were intermediate between the previous two mentioned composites and are less emphasized in the current study than the other three TCT environment types. An alternative stratification could have grouped LTCs in a 2 × 2 matrix of environment types based on TC intensity at landfall, and number of subsequent TCTs. However, this was an impractical strategy for composites, since category-2 or greater LTCs that produced <10 recorded

tornadoes were uncommon, with only 5 cases from 1995 to 2021 that were not exposed by virtue of their track to likely sampling biases discussed later in this section.

The n = 72 ALL–CASES composite, including all cases from the four TCT environment types (Table 1) was also constructed and is used to illustrate conditions for a more generic LTC. A fifth composite category exemplifying environmental conditions in cases with numerous TCTs occurring in well inland LTCs (>250 km from the coast and >24 h after landfall) was constructed from cases across the previous four environment types and is described in section 5.

TC tracks were determined from the International Best Track Archive for Climate Stewardship (IBTrACS; Knapp et al. 2010, 2018) and are plotted for cases included in the STRONG LTC–MANY TCTs, WEAK LTC–MANY TCTs, SOME TCTs, and FEW OR NO TCTs composites containing 16 (Fig. 1a), 23 (Fig. 2a), 13 (Fig. 3a), and 20 (Fig. 4a) cases, respectively. For each LTC, the strength of the TC at landfall is indicated next to the TC name and year in the figure legend (Figs. 1a, 2, 3a, and 4a). A 24-h postlandfall period selected for each TC included in the composites was based on the time window containing the most TCTs following landfall, where landfall itself was defined as the 3-hourly TC position closest in time to when the TC center first reached land. The LTC position during this 24-h period is indicated by the solid part of the track curve (Figs. 1a, 2a, 3a, 4a), and associated TCTs during the period are color-coded to match LTC tracks. The SOME TCTs and NO OR FEW TCTs environment types had no requirements on TC strength at landfall and contained 12 weak and 1 strong LTC (Fig. 3a), and 20 weak and 3 strong LTCs (Fig. 4a), respectively. Composites were also produced using the same sets of TCs for a 24-h period prior to landfall, during which either the entire or large majority of the TC circulation was located offshore. Postlandfall composites are compared to these prelandfall composites in section 4a.

Since this study seeks to determine 1) the spatial variability of environmental predictors for TCT production, and 2) the diurnal cycle of TCTs and their environmental predictors, an important consideration for case selection in the composites was the desirability for LTC tracks where much of the LTC circulation persisted over land during a diurnal cycle. This consideration motivated the exclusion from composites of many cases that otherwise met the forestated criteria for the STRONG LTC–MANY TCTs (Fig. 1b), WEAK LTC–MANY TCTs (Fig. 2b), SOME TCTs (Fig. 3b), and NO OR FEW TCTs (Fig. 4b) environment types.

Excluded were cases where LTCs tracked northeastward near the immediate southeastern or Mid-Atlantic coast, and if included could potentially result in undersampling the right side of LTCs (e.g., cases 1, 2, 6 in Fig. 1b, cases 1, 5, 8, 9 in Fig. 3b, and case 17 in Fig. 4b). where past studies have indicated the large majority of TCTs occur (e.g., McCaul 1991; Schultz and Cecil 2009; Edwards 2012; Edwards and Mosier 2022). Also excluded were cases where LTCs made landfall outside of the United States but produced many of their recorded TCTs over the United States (e.g., cases 4 and 5 in Fig. 1b, and case 1 in Fig. 4b). Another class of excluded cases occurred when LTCs moved across the Florida peninsula in less than 12 h (e.g., case 3 in Fig. 1b, case 5 in Fig. 2b, cases 3 and 7 in Fig. 3b, and cases 2, 5, 13, and 19 in Fig. 4b), which if included could potentially bias the diurnal cycle of TCTs. A final type of excluded case occurred when TCs produced their diurnal cycle of maximum TCTs while still located offshore (e.g., cases 2 and 6 in Fig. 2b, and case 6 in Fig. 3b), and thus could be accompanied by environmental conditions less broadly representative of typical LTC environments. The large number of excluded cases (44 excluded cases in Figs. 1b–4b compared to 72 retained cases in Figs. 1a–4a) suggests that such cases likely comprise important modes of TCT production worthy of further study. However, given the forestated objectives of the current study and large sampling uncertainties, these cases were deemed less amenable to spatiotemporal composites of TCT frequency and their mesoscale environmental conditions.

b. *Comparison of NARR output with NWS radiosonde data*

The gridded NARR output is available at 3-h intervals, has a horizontal spacing of about 32 km, and contains 29 pressure levels extending from 1000 to 100 hPa. A complete list of NARR variables may be found (at this writing) at https://psl.noaa.gov/gridded/data.narr.html.

In this section, we examine the suitability of using the NARR to characterize eastern U.S. TCT environments by comparing NWS radiosondes (Table A1 in the appendix) located on both the right and left sides of the LTC (relative to storm heading) for the 72 total cases plotted in Figs. 1a and 4a with corresponding vertical soundings obtained from the nearest NARR horizontal grid points. The right (left) sides of the LTC relative to the storm heading are most often the downshear (upshear) sides with respect to the environmental flow. We limit these comparisons to NWS radiosondes launched from 75 to 750 km of the LTC center. This aspect follows Schenkel et al. (2020), who noted that soundings within 75 km were often exposed to extreme winds, which could cause horizontal balloon drifts resulting in unreliable vertical shear estimates, and that soundings beyond 750 km were often located outside of the LTC circulation.

Surface temperature T_{sfc} (Fig. 5a) and dewpoint Td_{sfc} (Fig. 5b) from the NARR each have good correlations (R^2 = 0.72 and 0.62, respectively) with NWS soundings. The overall NARR T_{sfc} and Td_{sfc} biases (Table 2) are acceptably small at +0.4° and −0.4°C, respectively. Furthermore, the Td_{sfc} biases in both the right and left sectors (Table 2) were similarly modest with magnitudes of ≤1°C, which is much less than the ~3°C mean difference magnitudes between these regions in NWS soundings (Figs. 5a,b and Table 2).

At 850 hPa, near or slightly above the PBL top, the biases in equivalent potential temperature θ_e are similarly small (Table 2). Here, the larger bias of −1 K on the right side of the LTC is still significantly less than the 3.4-K observed average difference across the LTC (Table 2). These cases have large average differences in midtropospheric relative humidity between the right and left sides of the LTC (Fig. 5c, Table 2),

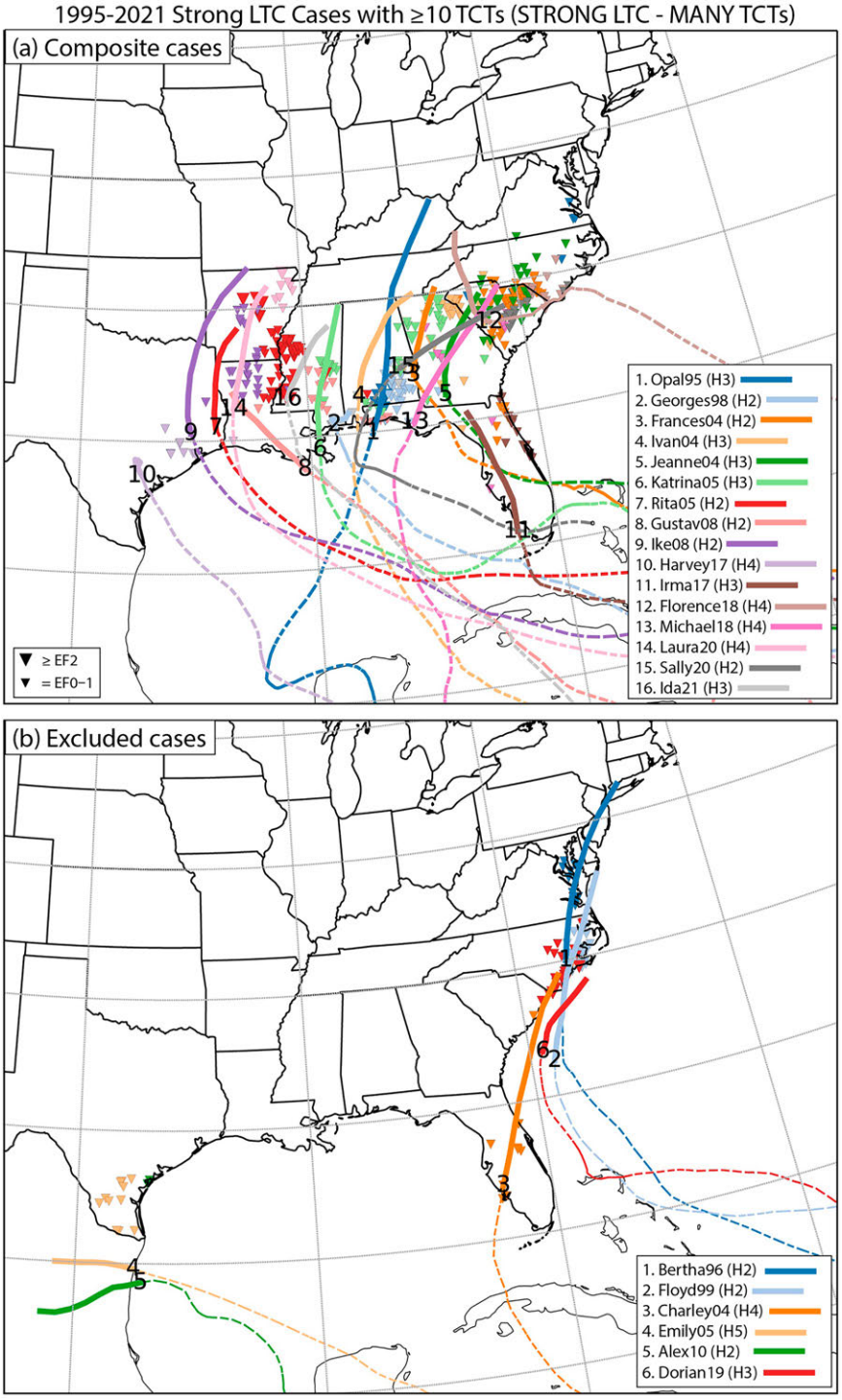

FIG. 1. Tropical cyclone tracks (a) selected and (b) excluded for composites of the STRONG LTC–MANY TCTs environment type (Table 1). The solid portion of the track includes the 24-h period used in the composite most tornadic diurnal cycle with the case number plotted at the beginning of the diurnal cycle. The color-coded tornado symbols represent the locations and intensities of TCTs during the diurnal cycle. The parenthetical entries provided in the legend of (a) indicate LTC intensities at the most recent landfall prior to the 24-h periods used in the composites (solid portion of TC tracks). For excluded cases in (b), corresponding intensities are for the time of first landfall along the solid portion of the TC tracks, or at offshore locations for cases that do not make landfall but produce TCTs on land.

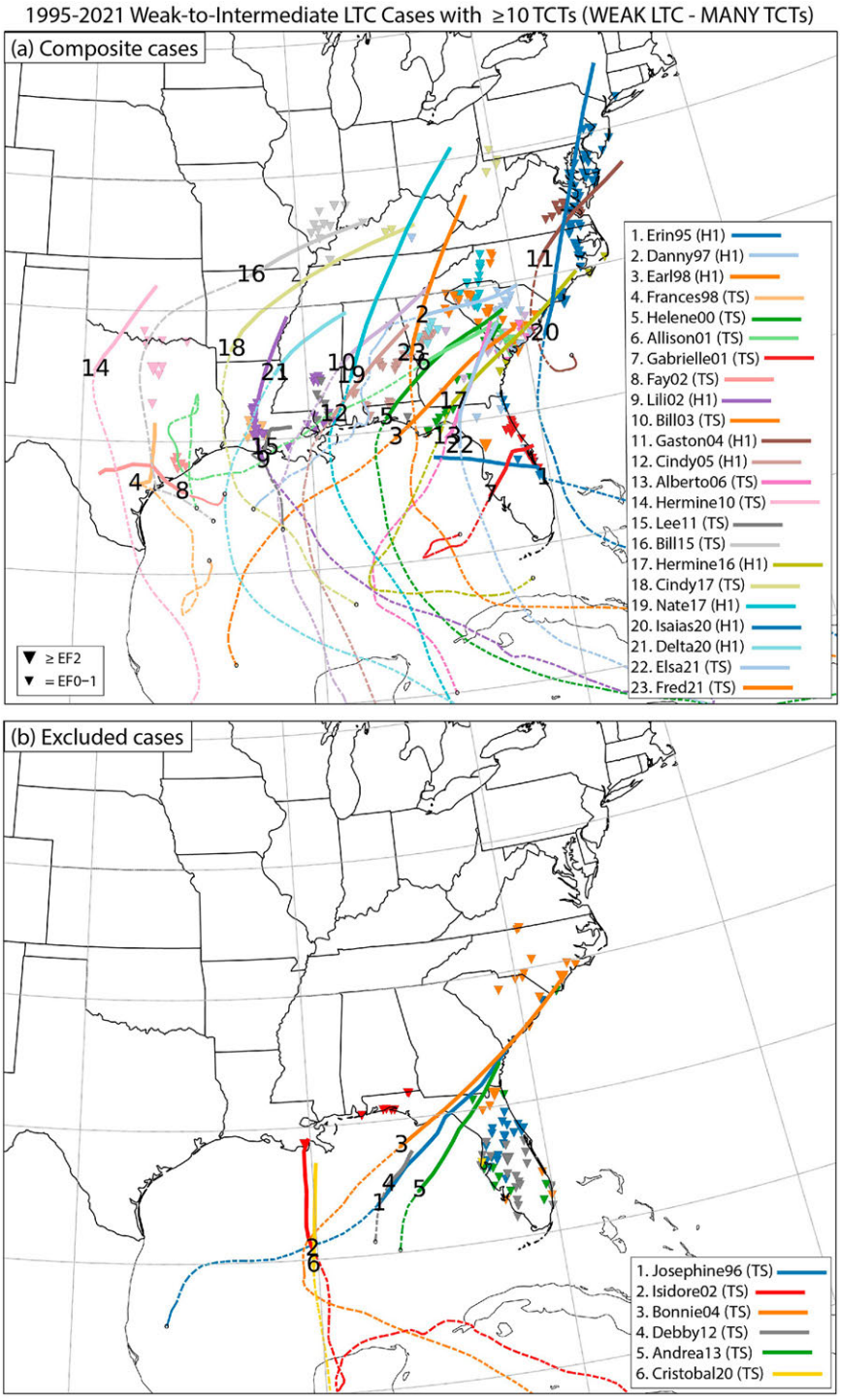

FIG. 2. As in Fig. 1, but for composites of the WEAK LTC–MANY TCTs environment type (Table 1).

which like for the surface moisture (Fig. 5b), are much larger than magnitudes of the NARR biases in these regions. The relatively small NARR biases in above-surface moisture for the current set of cases are likely linked to strong mesoscale horizontal advections and vertical motions within LTC circulations being adequately represented in the NARR (sections 4 and 5). Together, the lack of strong moisture biases from the surface through the middle troposphere support the small biases in column precipitable water (Fig. 5d, Table 2), which are very well correlated with observations.

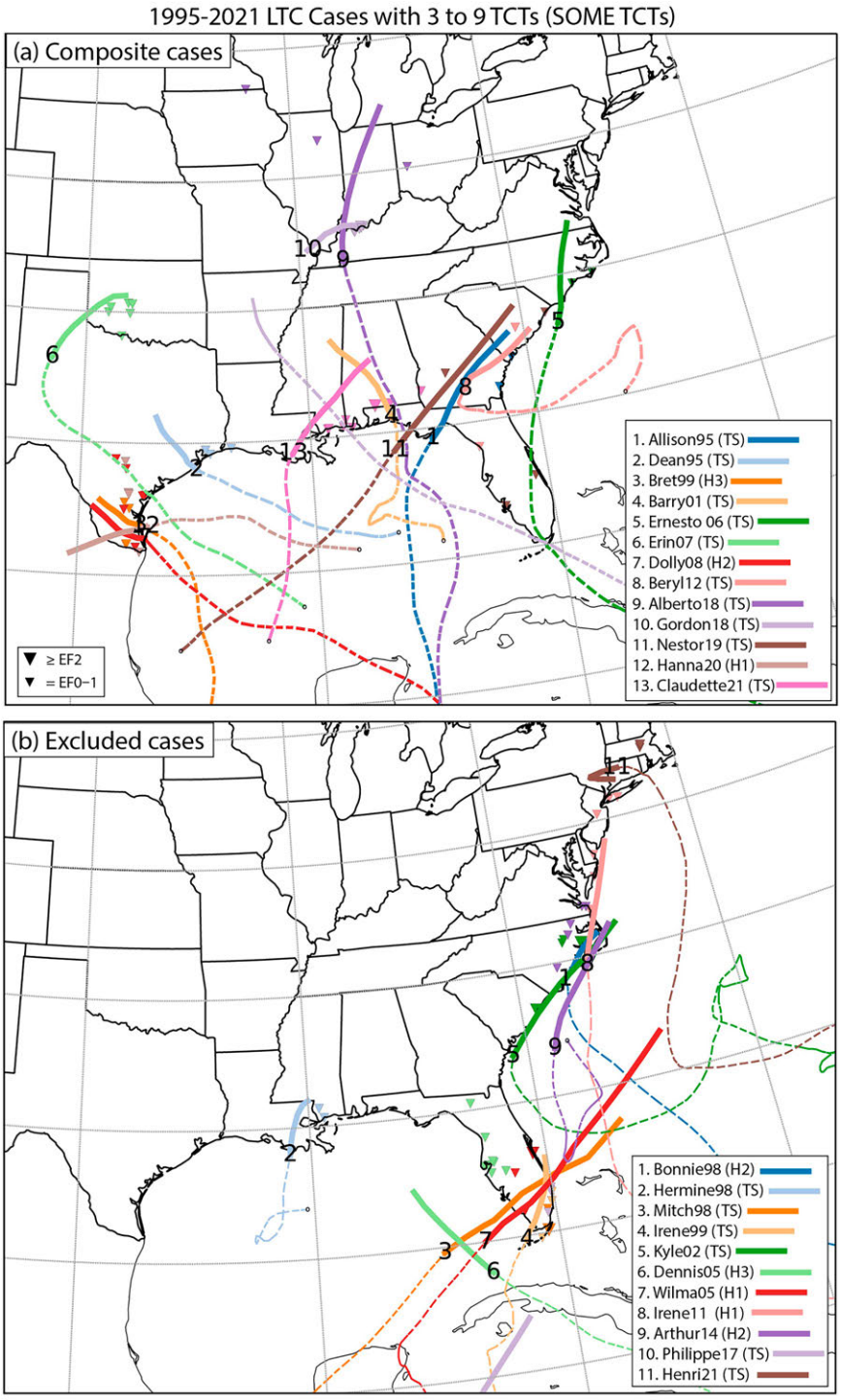

FIG. 3. As in Fig. 1, but for composites of the SOME TCTs environment type (Table 1).

Scatter diagrams of conventional severe weather parameters (e.g., Rasmussen and Blanchard 1998; Thompson et al. 2003, 2007) have also been constructed. These include mixed-layer CAPE (MLCAPE, Fig. 6a) calculated using virtual temperature averaged over the lowest 30 hPa, surface–3-km storm-relative helicity (SRH03, Fig. 6b), which uses the Bunkers et al. (2000) formula for cell motion, and the 10–1000- and 10–5000-m bulk wind differences, BWD01 (Fig. 6c) and BWD05 (Fig. 6d), used to characterize the vertical shear. Though NARR MLCAPE has only fair correlation with radiosondes

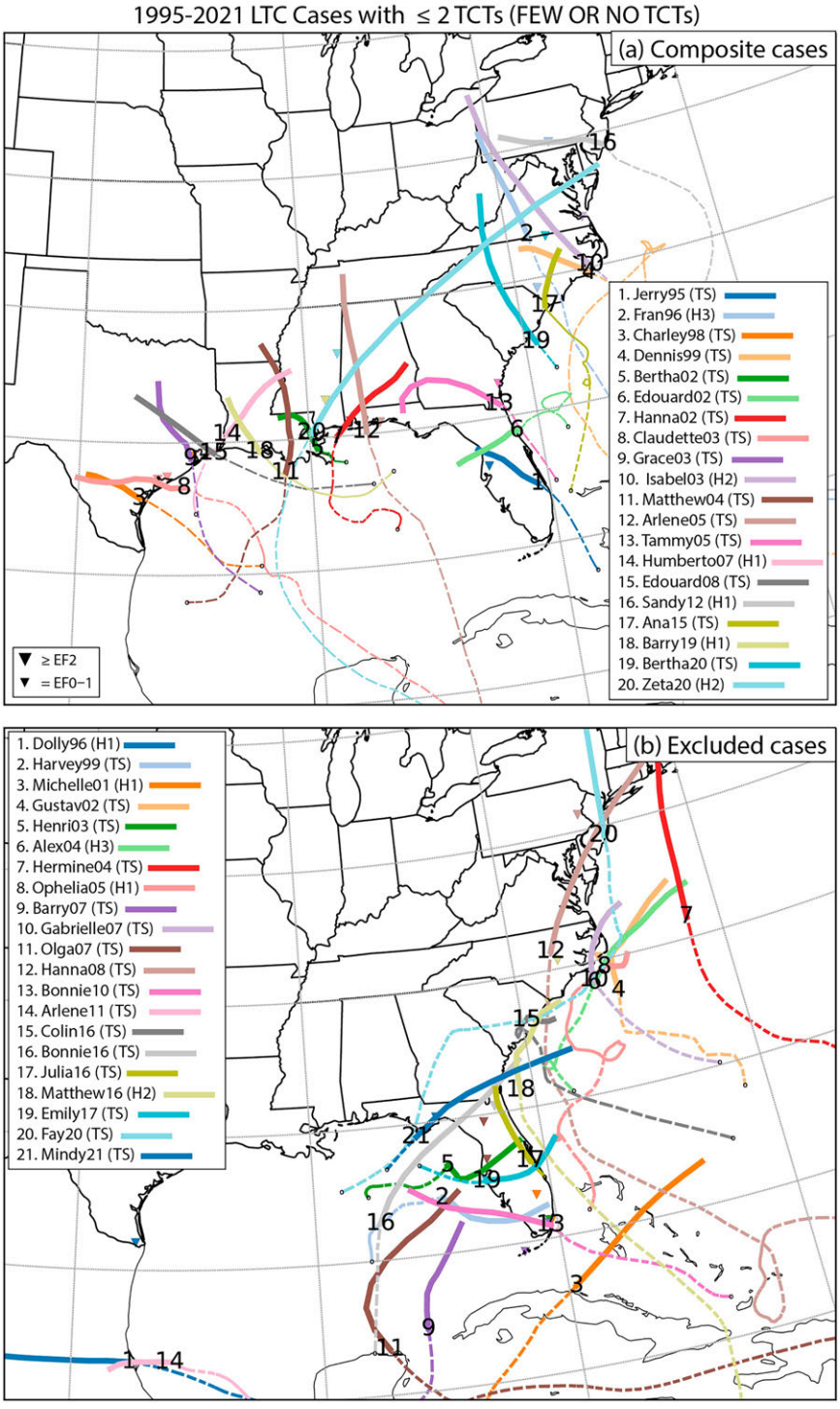

FIG. 4. As in Fig. 1, but for composites of the FEW OR NO TCTs environment type (Table 1).

and moderate-to-large absolute errors, the negative bias, which occurs both on the right and left sides of the LTC (Fig. 6a, Table 2), is small in comparison to observed average differences across the LTC. The NARR-based kinematic variables of BWD01, BWD05, and SRH03 are better correlated with their NWS radiosonde counterparts but have a more noticeable overall negative bias (Figs. 6b–d), which is most pronounced on the LTC's right side of the (Table 2). The negative bias is most significant for lower-tropospheric kinematic variables (i.e., BWD01, SRH01),

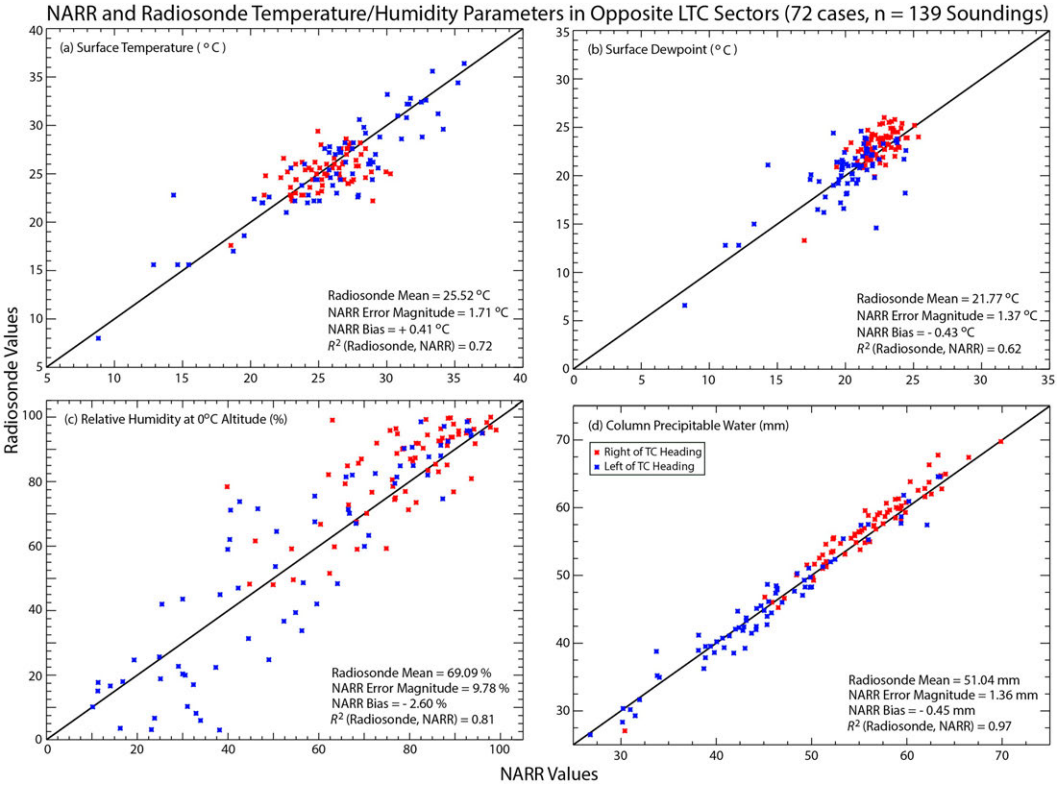

FIG. 5. Scatter diagrams of NWS radiosonde-observed and collocated NARR (a) surface temperature, (b) surface dewpoint, (c) relative humidity at the first 0°C level, and (d) column precipitable water for the sounding locations listed in Table A1 of the appendix, which comprise cases for which LTC tracks are plotted in Figs. 1a–4a. Red (blue) symbols indicate locations to the right (left) of these LTC tracks.

and may be partly related to inadequacies in NARR vertical resolution.

In summary, many of the NARR thermodynamic variables have fair to good correlations with their NWS radiosonde counterparts in our $n = 72$ TCT environment cases. Our analysis indicated that the NARR realistically captured average BWDs on the right side of LTCs that were enhanced relative to the left side. However, it revealed a substantial negative bias in the magnitudes of the 0–1-km vertical shear (BWD) and SRH in this location, which may also occur in severe weather environments diagnosed using operational mesoscale analysis systems (e.g., Coniglio and Jewell 2022). Apart from this caveat, the overall character of the TCT environments described in forthcoming analyses appears well represented by the NARR.

TABLE 2. Mean values from NWS radiosondes (Table A1 of the appendix), and absolute error and bias of selected parameters (first column) from NARR horizontal grid points located closest to all soundings (second column) and for those obtained within sectors to the right (third column) and left (fourth column) of the TC heading for TCT environments used in the composites ($n = 72$ LTC cases).

NARR parameter (units)	Total (139 soundings) mean, error, bias	Right of TC (71 soundings) mean, error, bias	Left of TC (68 soundings) mean, error, bias
PW (mm)	51.0, 1.4, −0.4	56.7, 1.4, −1.0	45.1, 1.3, +0.1
$RH_{0°C}$ (%)	69.1, 9.8, −2.6	83.8, 8.5, −5.3	53.7, 11.1, +0.3
850-hPa θ_e (K)	341.2, 2.0, −0.5	342.8, 2.0, −1.0	339.4, 2.0, +0.1
T_{sfc} (°C)	25.5, 1.7, +0.4	25.2, 1.6, +0.4	25.9, 1.8, +0.4
Td_{sfc} (°C)	21.8, 1.4, −0.4	23.2, 1.2, −0.7	20.3, 1.5, −0.2
MLCAPE (J kg^{-1})	724, 371, −157	945, 491, −250	493, 247, −61
SRH01 (m^2 s^{-2})	61, 45, −26	110, 66, −51	9, 23, +1
SRH03 (m^2 s^{-2})	80, 59, −23	124, 73, −43	34, 45, −1
BWD01 (m s^{-1})	11.5, 4.7, −4.2	14.9, 5.9, −5.5	7.9, 3.4 −2.8
BWD03 (m s^{-1})	12.3, 3.5, −2.8	15.5, 4.2, −3.4	9.0, 2.7, −1.5
BWD05 (m s^{-1})	11.9, 3.1, −1.3	15.8, 3.8, −2.7	8.0, 2.4, −0.9

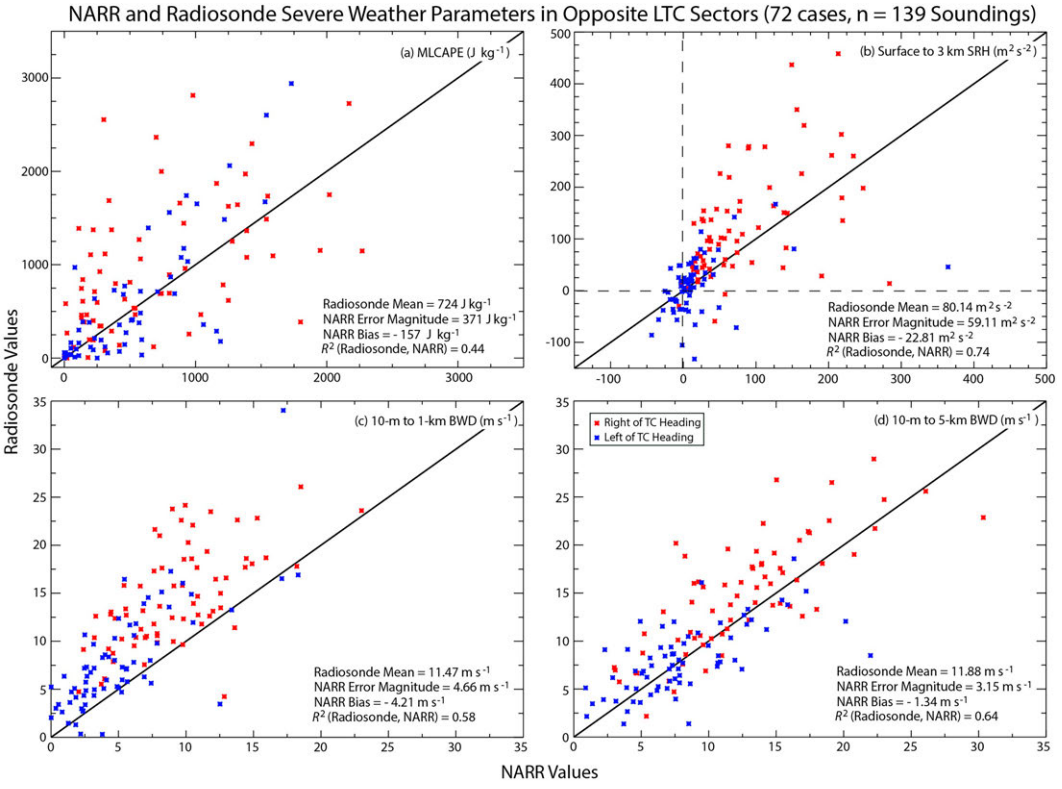

FIG. 6. As in Fig. 5, but for (a) mixed-layer CAPE, (b) surface–3-km storm-relative helicity, (c) surface–1-km (BWD01), and (d) surface–5-km (BWD05) bulk vertical wind difference magnitudes.

c. *NARR composite methodology*

Gridded NARR output at 3-h intervals were used to construct the composites. To discern TCT associations with different environmental variables, reports from the TCTOR archive are plotted for a 3-h time window centered on the time of each of the 3-hourly NARR composites. In addition, composites were averaged for daytime (1500, 1800, 2100, 0000 UTC) and nocturnal (0300, 0600, 0900, 1200 UTC) periods, and diurnal averages were also produced by including each of the eight NARR daily output times.

To construct the composites, gridded NARR fields were mapped to polar coordinates centered on instantaneous TC locations, which were determined from IBTrACS. Composites were produced for three different coordinate systems and an example of diurnally averaged 700-hPa winds for the ALL–CASES environment is shown in Fig. 7. These systems include a geographically fixed coordinate with north (N) pointing up (Fig. 7, left panels), and a TC-heading based coordinate with the direction of TC motion (front), which was determined from IBTrACS, pointing up (Fig. 7, middle panels). To convert from Earth-relative to TC-heading coordinates we rotated the gridded NARR data so that the TC-heading azimuth was pointing upward (360° on the compass) for each individual case prior to averaging for composites. The reasonably close correspondence of the TCTs and mean 700-hPa wind locations between the fixed (Fig. 7, left panels) and TC-heading relative (Fig. 7, middle panels) coordinates is consistent with the approximate northward direction of the mean LTC motion vector (from 199° at 4.89 m s^{-1}) for the diurnal average of the postlandfall ALL–CASES composite.

Schenkel et al. (2020, 2021) and others have emphasized the importance of the environmental vertical shear magnitude through the TC depth in determining the frequency and intensity of TCTs, which are climatologically maximized downshear of the TC center. This motivates our choice of a third coordinate system (Fig. 7, right panels), which is based on the 850–200-hPa environmental vertical shear, with the downshear (DS) direction pointing up. Here, we follow the approach employed in previous studies (e.g., Davis et al. 2008; Galarneau and Davis 2013; Schenkel et al. 2020) and remove the winds associated with the TC by subtracting rotational and irrotational winds within 500 km of the TC center from the total TC wind at 850 and 200 hPa at corresponding grid points. The resulting winds from these pressure levels are vertically differenced and horizontally averaged to obtain the environmental shear direction.

The locations of TCTs and the 700-hPa wind patterns (Fig. 7, right panels) are rotated more substantially from corresponding plots in TC-heading relative coordinates than are those from the ground-relative coordinates. This rotation is consistent with the mean 850–200-hPa environmental BWD vector (from 254° at 9.92 m s^{-1}), which has a heading 74° to the right of north (Fig. 7, left panels) and 55° to the right of that for the mean LTC motion (Fig. 7, middle panels) for the diurnal average of the postlandfall ALL–CASES composite.

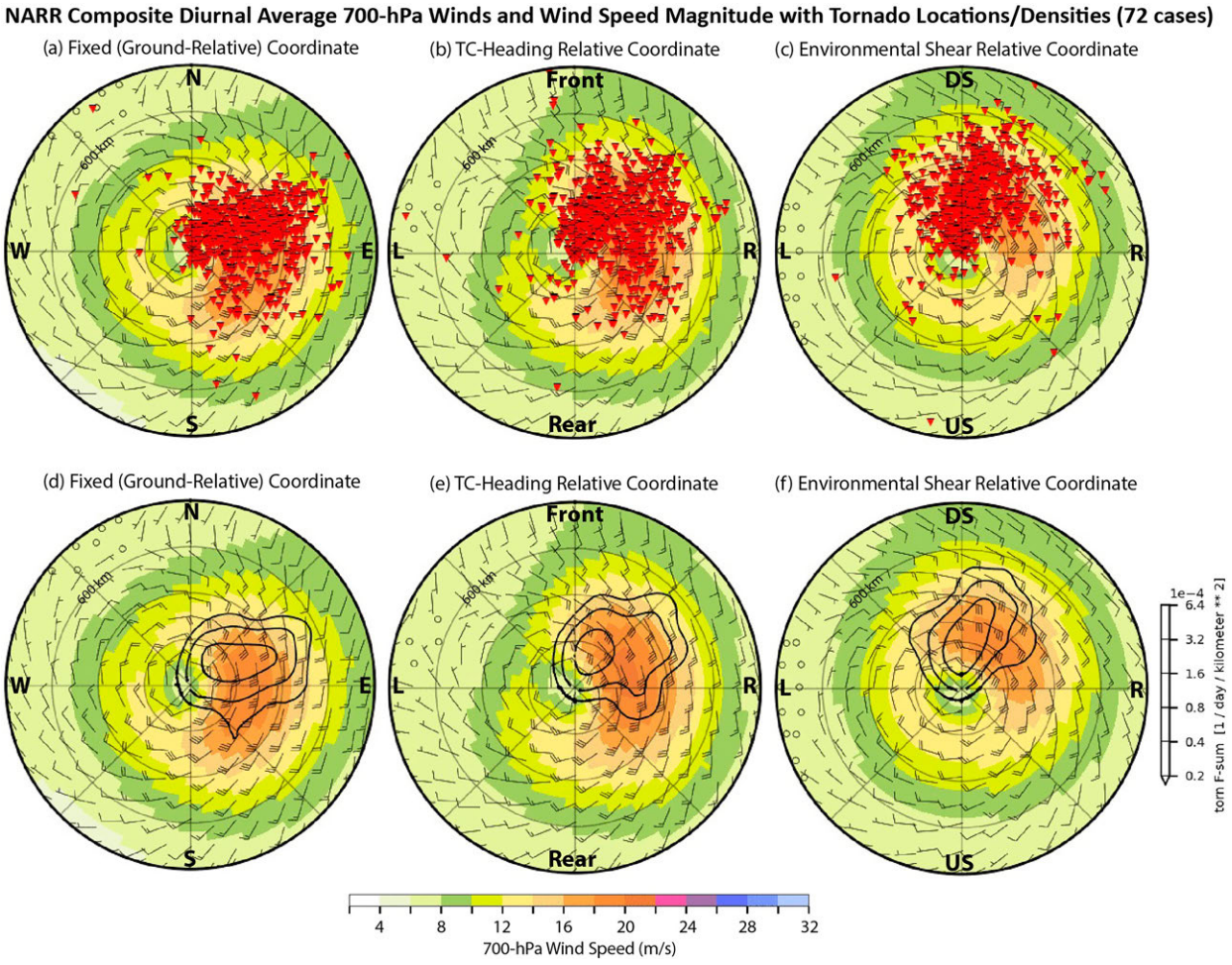

FIG. 7. Diurnally averaged NARR 700-hPa winds and wind speed magnitude (color shading) for the $n = 72$ ALL–CASES composite with (top) TCT locations (larger triangles are ≥EF2-rated, smaller triangles are ≤EF1) during the 24-h diurnal cycle of maximum TCT frequency and (bottom) F-sum tornado density field (see text) in black contours (scale at lower right) overlaid for (a),(d) ground-relative; (b),(e) tropical-cyclone heading relative; and (c),(f) 850–200-hPa environmental shear relative coordinates, where the top points north (N), in the direction of TC motion (front), and downshear (DS), respectively. The wind barbs are plotted using the standard meteorological convention (circle < 2.5 kt, half barb = 5 kt, full barb = 10 kt, pennant = 50 kt; 1 kt = 0.514 m s^{-1}).

A tornado density field (Figs. 7d–f) enables correlations with environmental predictor fields derived using NARR output (section 4) to be examined and facilitates visualization of the spatial relationships among TCT frequencies and these environmental predictor fields. To construct the tornado density field, we employ a kernel-density estimate (KDE) of the true probability density function (PDF) of a random variable using the scipy Python module (Virtanen et al. 2020) function "stats.gaussian_kde, v1.9.1." The KDE is the sum of two-dimensional Gaussian kernels centered on TCT report locations. The kernels' size and orientation are determined by the overall covariance of the report locations and the *effective* number of points as described by stats.gaussian_kde. To emphasize more intense tornadoes, the TCT report locations are weighted by their F sum (McCaul 1991; Eastin et al. 2014), which is the enhanced Fujita (WSEC 2006) damage rating (EF) magnitude + 1. The F-sum tornado density fields corresponding to tornado plot symbols in Figs. 7a–c pinpoint local maxima in the northeast (Fig. 7d), right front (Fig. 7e), and the downshear-right (Fig. 7f) quadrants for the three different coordinate systems.

3. Diurnal cycle of TCT environments

McCaul (1991) showed that TCT distance from the center of LTCs has a broad distribution, with maximum frequencies about 300 km from the LTC center, and a small secondary maximum located much closer to the center (their Fig. 13). The TCTs occurring outside of the TC inner core, which are often associated with discrete supercells (e.g., McCaul 1991; Edwards at al. 2012), have a pronounced diurnal cycle with maximum frequency in the afternoon. In the remainder of the paper, we focus on the TCT environments outside of the TC inner core (i.e., from $r = 50$ to 750 km of the TC center), since

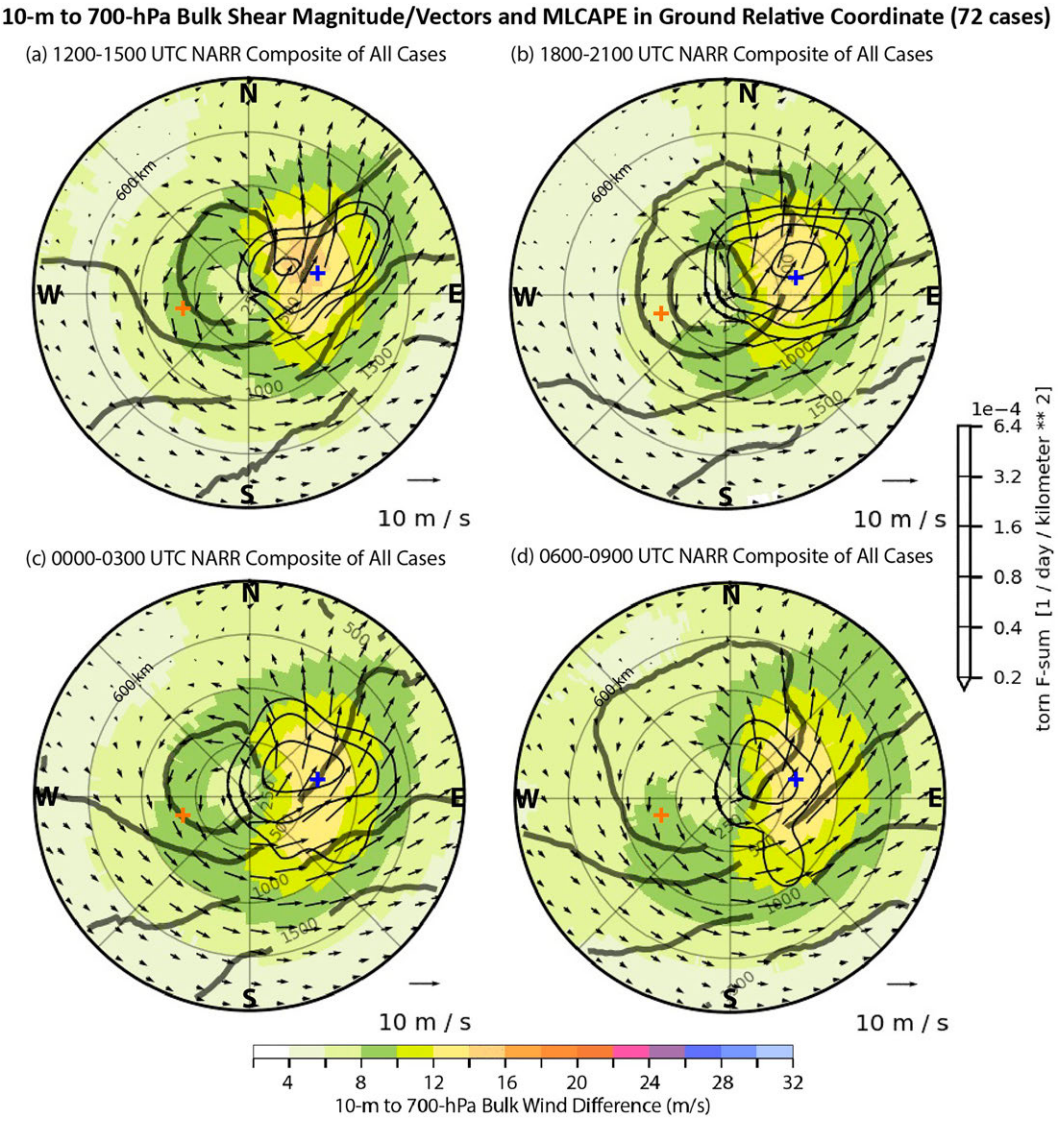

FIG. 8. Diurnal cycle of 10-m–700-hPa BWD magnitude (color shading) and vectors, MLCAPE (250, 500, 1000, and 1500 J kg^{-1} contours in bold gray), and the F-sum tornado density field (thin black contours with values indicated at right) for $n = 72$ ALL–CASES composite in ground-relative coordinates. The color-coded cross symbols indicate the locations of the composite soundings, and time series presented in Figs. 9 and 10, respectively.

those TCTs are more common and have supporting environmental conditions that are easier to discern from reanalyses, consistent with locations of the NARR-NWS sounding pairs (Table A1) analyzed in section 2b.

In this section we illustrate the general aspects of the TCT diurnal cycle and environment using the 72-member ALL–CASES composite (Fig. 8). Consistent with previous studies, TCTs are most common during the early afternoon several hundred km from the LTC center. In ground-relative coordinates (Fig. 8), they are centered near the composite mean lower-tropospheric vertical shear maximum along the east and northeast sides of the LTC circulation. This vertical shear is a combination of the background environmental shear (section 2c) that increases after TC landfall (Table 3) and vertical shear associated with the TC circulation, which focuses maximum net 10-m–700-hPa BWDs to the right side of the TC center.

The structure of the composite mean MLCAPE field is influenced by horizontal moisture advection within the LTC circulation, which biases maximum values to the right side of the storm center (Fig. 8). MLCAPE decreases throughout the LTC circulation overnight (Fig. 8), and likely influences the overall concurrent decreasing TCT frequency within LTC, despite similar maximum values of 10-m–700-hPa BWD (Figs. 8b,d). However, there are small local increases in 10-m–700-hPa BWD in the southeast quadrant of the LTC starting during the evening and persisting overnight (Figs. 8c,d), which are consistent with a southward extension of the outer contour of TCT frequency overnight (Fig. 8d) despite locally decreasing values of MLCAPE.

TABLE 3. Evolution of the diurnally averaged 850–200-hPa environmental bulk wind difference (BWD) magnitudes and azimuths from prelandfall to postlandfall time periods for different composite TCT environment types. The parenthetical values in the final two rows are the number of postlandfall cases (second column) and their average BWD magnitude and azimuth (fourth column) for TCT environment types that included some cases for which full prelandfall diurnal cycles could not be constructed due to TC onset occurring less than 24 h prior to landfall. Diurnally averaged pre- to postlandfall BWD magnitude and azimuth changes (fifth column) are based on identical prelandfall and postlandfall cases and their composite averages (listed outside of parentheses).

TCT environment type	Cases	Prelandfall environment 850–200-hPa BWD (m s^{-1}, ° azimuth)	Postlandfall environment 850–200-hPa BWD (m s^{-1}, ° azimuth)	Change (m s^{-1}, ° azimuth)
STRONG LTC–MANY TCTs	16	5.86, 257°	11.79, 240°	+5.93, −17°
WEAK LTC–MANY TCTs	23	8.07, 273°	12.28, 253°	+4.24, −20°
SOME TCTs	13	5.42, 265°	9.03, 276°	+3.61, +11°
FEW OR NO TCTs	(20) 17	6.12, 275°	(7.05) 7.53, (255°) 262°	+1.41, −13°
ALL CASES	(72) 69	6.52, 269°	(9.92) 10.17, (254°) 255°	+3.65, −14°

Both the lower-tropospheric hodograph curvature and MLCAPE are substantially greater near the location of maximum evening TCT frequency (Fig. 9a), about 250 km from the LTC center (blue cross in Fig. 8c), than at the same distance (Fig. 9b) on the opposite side of the LTC (orange cross in Fig. 8c). Figure 10 displays a diurnal time series of both the composite mean (solid lines) and the 5th–95th percentiles generated from 10 000 bootstrap samples (shadings) used to estimate confidence intervals for the means in different locations of the LTC. Though MLCAPE values are modest throughout the diurnal cycle, the separation of the blue shaded band from the orange color band reveals statistical significance of the greater MLCAPE (Fig. 9a) in the downshear location (blue crosses in Fig. 8) than on the opposite side of the LTC throughout the diurnal cycle. Though it has less of a diurnal cycle, the differences in the 10-m–700-hPa BWD across the LTC are greater (Fig. 10b) than for MLCAPE (Fig. 10a), with BWD magnitudes near the TCT maximum about 75% larger than those at the same distance on the opposite side of LTC.

The moist near-surface conditions overlaid by approximate moist adiabatic lapse rates in the composite soundings (Fig. 9) are consistent with small average values of mixed-layer convective inhibition (MLCIN). The MLCIN (Fig. 10c) also has a weak diurnal cycle near the location of the daily average maximum TCT frequency (blue curve), consistent with persistent mesoscale ascent in this region (section 4a). However, mean

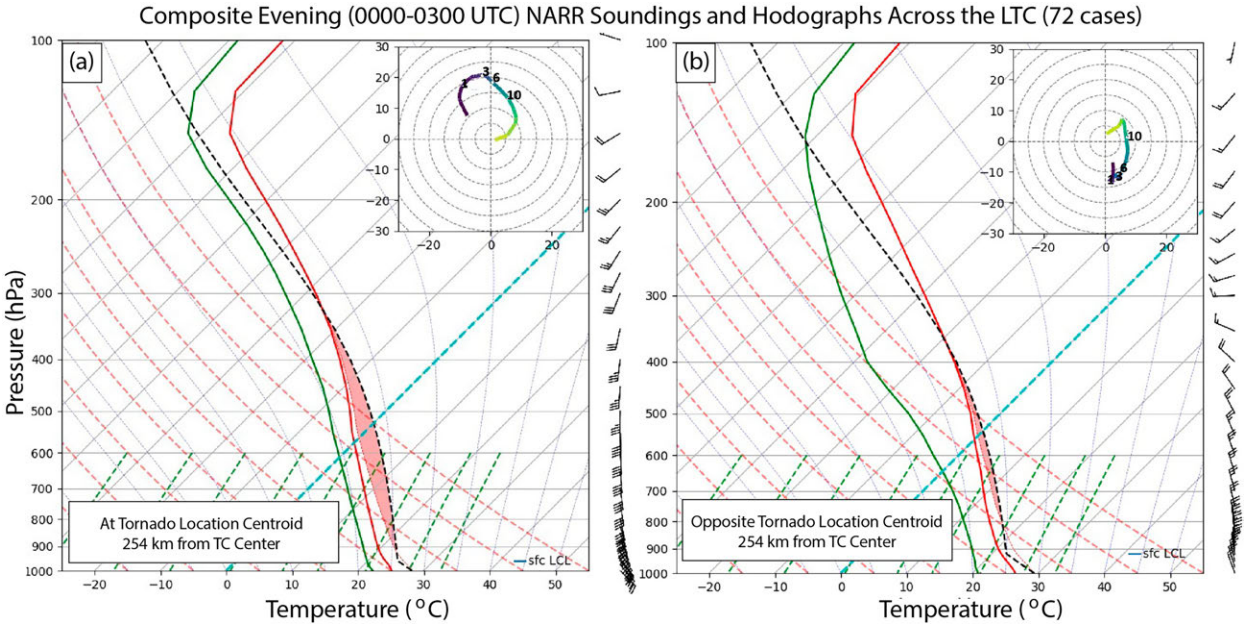

FIG. 9. Vertical profiles of skew T–log$p$ temperature and dewpoint (bold solid red and green curves, respectively) and hodographs (insets, with heights in km, and u, v wind components in m s^{-1} annotated) averaged from 0000 to 0300 UTC for the $n = 72$ ALL–CASES composite at (a) the approximate tornado location centroid (blue cross symbols in Fig. 8), and at (b) the corresponding location on the opposite side of the LTC (orange cross symbols in Fig. 8). The thin red curves denote vertical profiles of environmental virtual temperature, and the dashed black curves in each panel indicate pseudoadiabatic ascent trajectories for a mixed-layer air parcel. The red shaded regions are proportional to values of MLCAPE.

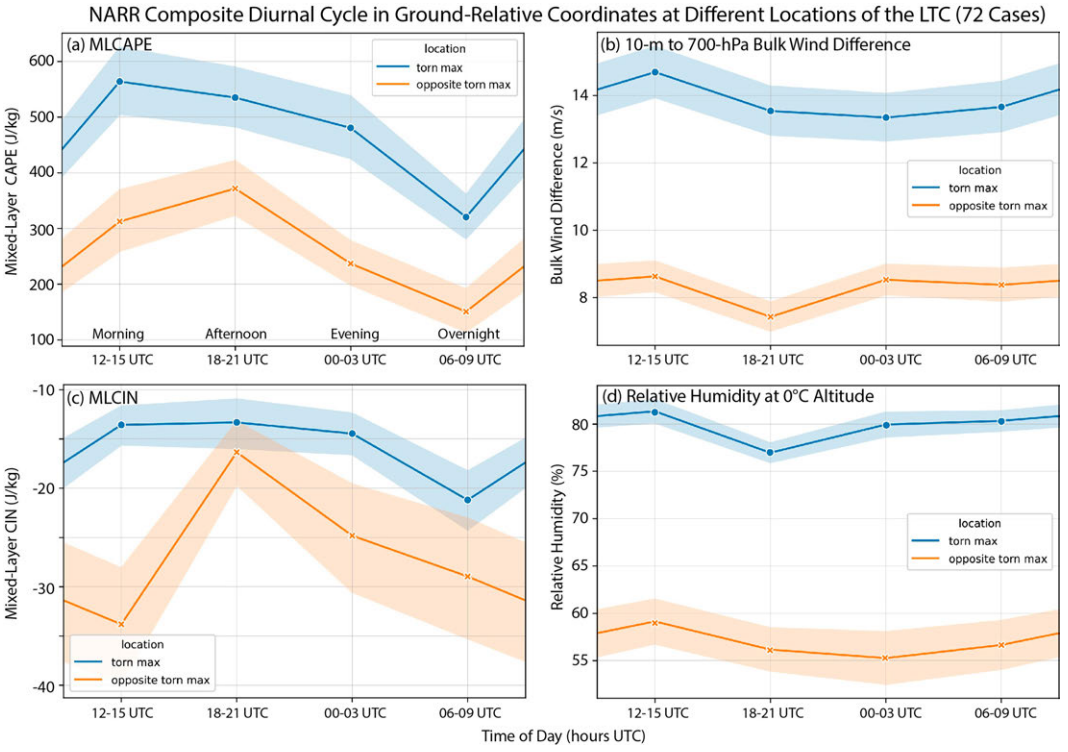

FIG. 10. Time series plots of mean (a) MLCAPE, (b) 10-m–700-hPa BWD magnitude, (c) mixed-layer convective inhibition (MLCIN), and (d) 0°C relative humidity from the $n = 72$ ALL–CASES composite at the locations specified by the blue (tornado centroid), and orange (opposite tornado centroid) cross symbols plotted in Fig. 8. The color-shaded bands comprise the 95% confidence interval for the mean, which is generated from 10 000 bootstrap samples.

MLCIN differences between the TCT maximum (blue shading) and the location equidistant from the LTC center but on its opposite side (orange shading) are not statistically significant for portions of the diurnal cycle. Like for the BWD (Fig. 10b), there are large statistically significant increases in midtropospheric relative humidity near the TCT maximum compared to the opposite side (Fig. 10d).

4. Mesoscale environmental conditions in contrasting TCT environments

By constructing composites for different TCT environments (Table 1) we sought to compare 1) differences between environments associated with many TCTs in strong LTCs with those in weaker LTCs, and 2) discern differences in environments between prolific tornado producing LTCs and those that produced few or no tornadoes. During the diurnal cycle immediately prior to TC landfall, average maximum 10-m winds are maximized in quadrants located to the right of storm motion for composites of different environment types (Fig. 11). These maximum 10-m AGL winds are 8–10 m s^{-1} stronger in the STRONG LTC–MANY TCTs composite (Fig. 11a) than in the WEAK LTC–MANY TCTs composite (Fig. 11b). In the FEW OR NO TCTs composite (Fig. 11c), 3 (15%) of its members had ≥ category-2 hurricane strength winds at landfall, which contributed to slightly stronger (~1–2 m s^{-1}) maximum winds than in the WEAK LTC–MANY TCTs composite (Fig. 11b). By having similar average LTC strengths at landfall, comparison of these composites facilitates objective 2 of examining the environmental factors favoring TCT production that may be less dependent on LTC strength at landfall.

a. *Effects of TC landfall on TCT environments*

Friction reduces the magnitude of the near surface winds after TC landfall for all cases, but especially for the STRONG LTC–MANY TCTs composite where the average 10-m AGL wind speed reduction is greatest among different TCT environment types (not shown). In STRONG LTC–MANY TCTs, the maximum local speed reductions on the right side of the LTC at 10 m AGL are 8–9 m s^{-1} (Figs. 12a,d), which contrasts with negligible changes in corresponding wind speed magnitudes at 700 hPa (cf. Figs. 12b,e). These differences contribute to large enhancements in the lower tropospheric vertical shear after TC landfall (Figs. 12c,f). In this composite of strong LTCs, the post-landfall diurnally averaged F-sum tornado density maximum lies within the diurnally averaged 10-m–700-hPa vertical shear maximum (Fig. 12f). The area of large tornado density extends from the right-front quadrant, where the 10-m–700-hPa BWD is maximized and local vertical shear is southerly, into the right-rear quadrant where MLCAPE is larger, and the local vertical shear is southwesterly (Fig. 12f).

Corresponding pre and postlandfall composites of 700-hPa pressure vertical velocity ω in TC-heading relative coordinates

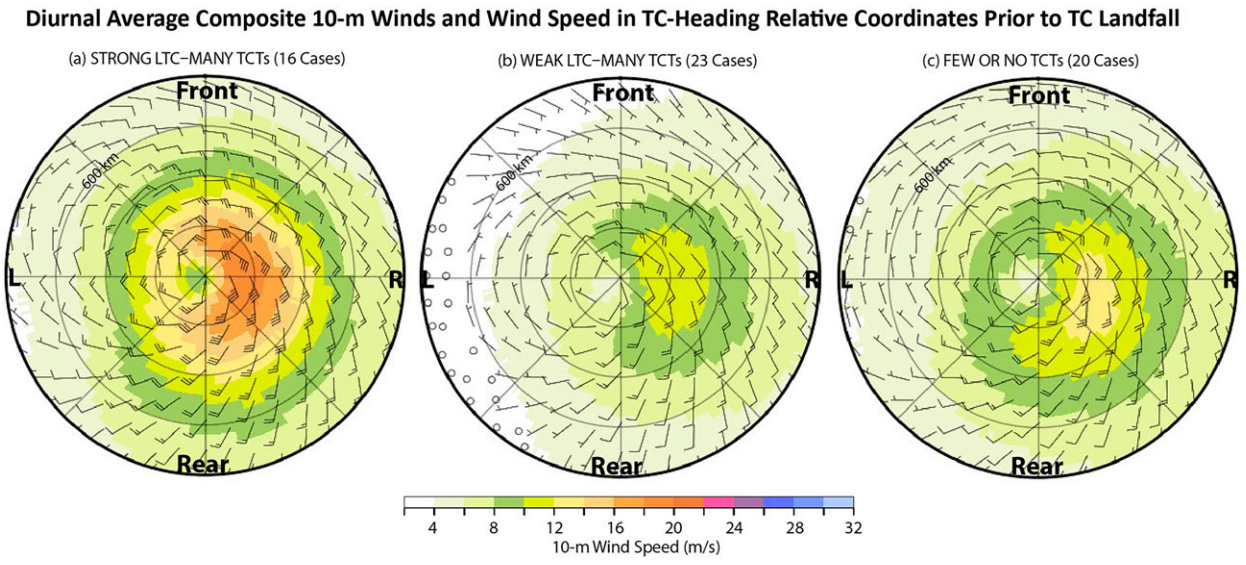

FIG. 11. Diurnal average of 10-m winds and speed magnitudes (color shading) for the (a) STRONG LTC–MANY TCTs (b) WEAK LTC–MANY TCTs, and (c) FEW OR NO TCTs composite environments (Table 1) in TC-heading relative coordinates immediately prior to TC landfall. The wind barbs follow the standard meteorological plotting convention used in Fig. 7.

show an evolution from a mesoscale ascent maximum near the TC center (Fig. 13a) to a more asymmetric vertical motion couplet after TC landfall (Fig. 13b). Schenkel et al. (2020, their Fig. 2) and others have illustrated how increases in the environmental vertical shear can influence secondary vertical circulations within TCs. As in the TC-heading relative coordinates, the 700-hPa mesoscale ascent maximum near the TC center evolves to a more asymmetric couplet after landfall in environmental shear coordinates (Figs. 13c,d), with ascent and descent, respectively, maximized downshear and upshear of the TC center. The net vertical shear increases are influenced by large frictionally induced surface wind decreases in the right front (RF) quadrant, which coincide with maximum TCT frequencies (cf. Figs. 13a,b). These vertical shear increases appear to be further augmented by the postlandfall increases in environmental vertical shear above the PBL as indicated in Table 3. Though most pronounced for the current 16-case STRONG LTC–MANY TCTs composite, vertical motion couplets oriented approximately along the environmental vertical-shear vector also occur in the other composites (not shown).

b. *TCT environment predictors*

Following McCaul (1991), who constructed composite contour maps of F-Sum and TCT environmental predictors from sounding data following TC motion, we compare diurnally averaged F-Sum tornado density and environmental variables from NARR reanalyses for the STRONG LTC–MANY TCTs (Fig. 14a), WEAK LTC–MANY TCTs (Fig. 14b), and FEW OR NO TCTs (Fig. 14c) environmental composites in TC-heading relative coordinates. The STRONG LTC–MANY TCTs composite has an average of 22 TCTs in the most tornadic diurnal cycle, which is the greatest of any environment type (Table 1), and ranges from 9 to 60 with a median of 17 among its 16 cases. The corresponding diurnal cycle of the WEAK LTC–MANY TCTs composite has an average of 12 TCTs (Table 1) and ranges from 5 to 39 with a median of 9 among its 23 cases. The F-sum maximum is located near the maximum 10-m to 500-hPa bulk wind difference (BWD500) in the RF quadrant for both composites having many TCTs (Figs. 14a,b). The maximum BWD500 in the STRONG LTC–MANY TCTs composite (~20 m s^{-1}) is greater than in WEAK LTC–MANY TCTs composite (~14–16 m s^{-1}), which in turn is stronger than in the FEW OR NO TCTs composite (~10–12 m s^{-1}) (Figs. 14a–c). Much stronger postlandfall 850–200-hPa environmental shear in WEAK LTC–MANY TCTs than in NO OR FEW TCTs (Table 3) is a factor that could increase the overall vertical shear (cf. Figs. 14b,c) and influence TCT greater frequencies in the former (Fig. 14b) despite slightly weaker average TC strength at landfall (Figs. 11b,c). Another important difference between WEAK LTC–MANY TCTs and FEW OR NO TCTs composite environments that could also influence TCT frequencies is the much larger average MLCAPE in the RF quadrant of the former (Figs. 14b,c).

Major structural characteristics of the NARR environmental and TCT density fields in the TC-heading relative coordinate (Figs. 14a–c) are similar in the ground-relative coordinate (Figs. 14d–f). For instance, the maximum tornado density and its proximity to the BWD500 maximum in the northeast quadrant for composites of environments supporting many TCTs (Figs. 14d,e) correspond well to those in the RF quadrants in the TC-heading relative coordinate (Figs. 14a,b). Because of similarities in the TCT density maxima and related NARR environmental features in the RF and northeast quadrants, and the more common use of ground-relative frameworks in forecasting applications, subsequent spatial analyses of TCT environments are presented in ground-relative coordinates unless otherwise indicated.

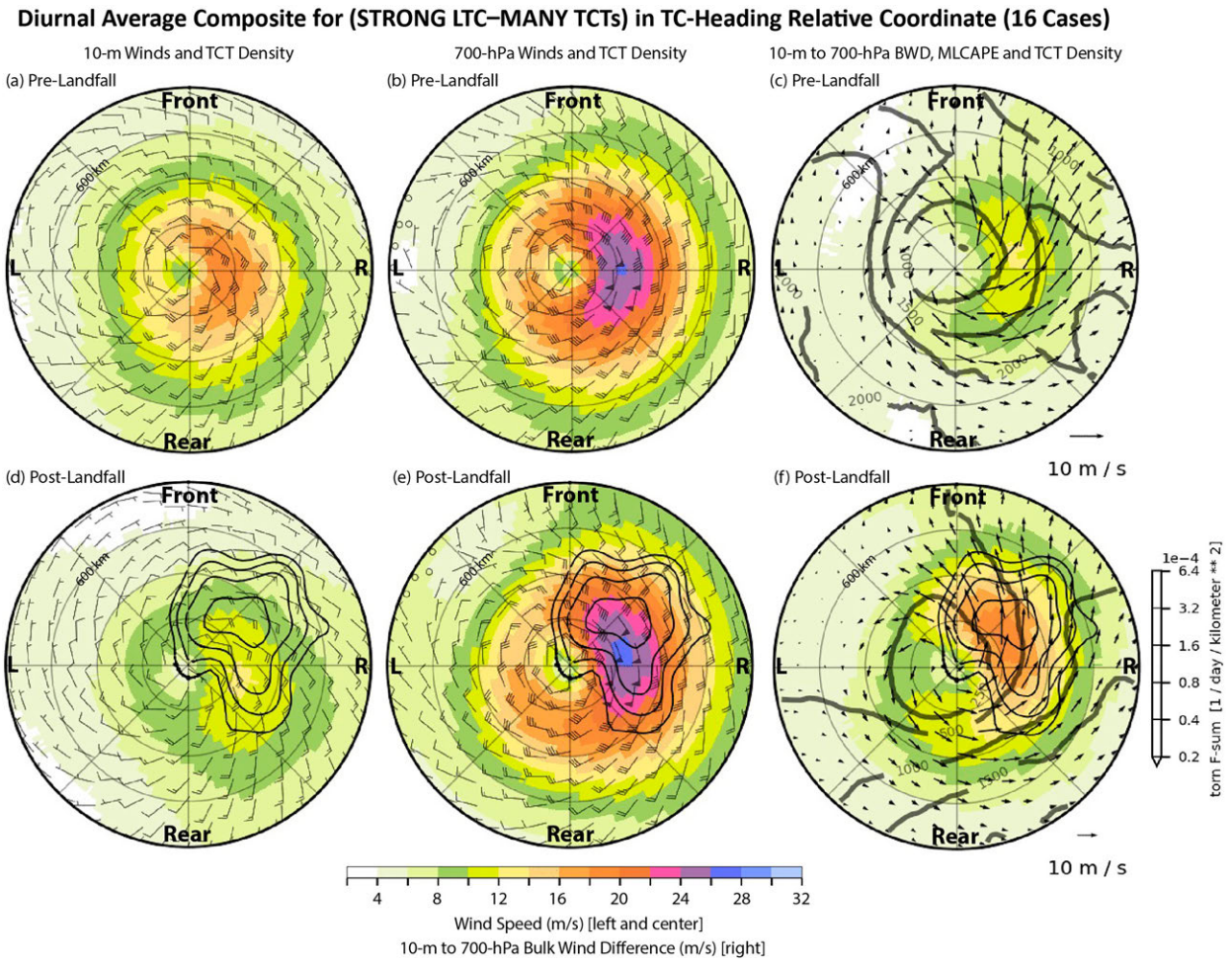

FIG. 12. Diurnally averaged F-sum tornado density (thin black contours, scale at lower right), and STRONG LTC–MANY TCTs environment composites in TC-heading relative coordinate (up points in direction of TC motion) of (left) 10-m winds and wind speed magnitude (a) prior to and (d) after TC landfall, (middle) 700-hPa winds and wind speed magnitude (b) prior to and (e) after TC landfall, and (right) 10-m–700-hPa BWD magnitude and vectors, and surface-based CAPE (thick gray contours of 250, 500, 1000, 1500, and 2000 J kg^{-1}) (c) prior to and (f) after TC landfall. The wind barbs in (a), (b), (d), and (e) follow the standard meteorological plotting convention in Fig. 7. The post-landfall phase (bottom) is for the most tornadic 24-h period following landfall indicated by the solid part of TC tracks in Fig. 1a.

The storm-relative helicity (Davies-Jones et al. 1990),

$$\mathrm{SRH} = \int_0^h \left[(\mathbf{v} - \mathbf{c}) \cdot \left(\mathbf{k} \times \frac{\partial \mathbf{v}}{\partial z} \right) \right] dz, \qquad (1)$$

is calculated through the lowest 3 km (SRH03)[1] for the STRONG LTC–MANY TCTs, WEAK LTC–MANY TCTs, and FEW OR NO TCTs environments (Fig. 15) using a storm motion vector **c** estimated with the Bunkers et al. (2000) formula for supercell motion. For the STRONG LTC–MANY TCTs composite, SRH03 has large maximum values of >300 m^2 s^{-2} located primarily in the northeast quadrant (Fig. 15a), which are comparable to SRH01 values from proximity soundings in TCT environments reported by Edwards et al. (2012) but may be somewhat underestimated based on possible NARR biases discerned from Fig. 6b. Though considerably less than the maximum values in the STRONG LTC–MANY TCTs composite, the maximum composite SRH03 values in the WEAK LTC–MANY TCTs composite (Fig. 15b) of 200–250 m^2 s^{-2} are supportive of tornadoes in general (e.g., Stensrud et al. 1997; Thompson et al. 2003) and exceed those from the FEW OR NO TCTs composite (Fig. 15c). The lack of TCTs in the latter despite at least marginal overall maximum SRH03 values > 150 m^2 s^{-2} (Fig. 15c) may be influenced by the small

[1] Recent work with newer reanalyses having greater near-surface vertical resolution, including the ERA5 (Coffer et al. 2020), has indicated that shallower layers (e.g., 0–500 m) are better at discriminating between tornadic and nontornadic conditions for general severe weather environments in the United States and Europe. We use the deeper 0–3-km SRH layer in the current study because, unlike for shallower SRH layers, SRH03 is directly output from the NARR, and NARR vertical wind shear and SRH have larger apparent biases when compared to NWS radiosondes for shallower layers (e.g., SRH01) than for the 0–3-km layer (Table 2, Fig. 6).

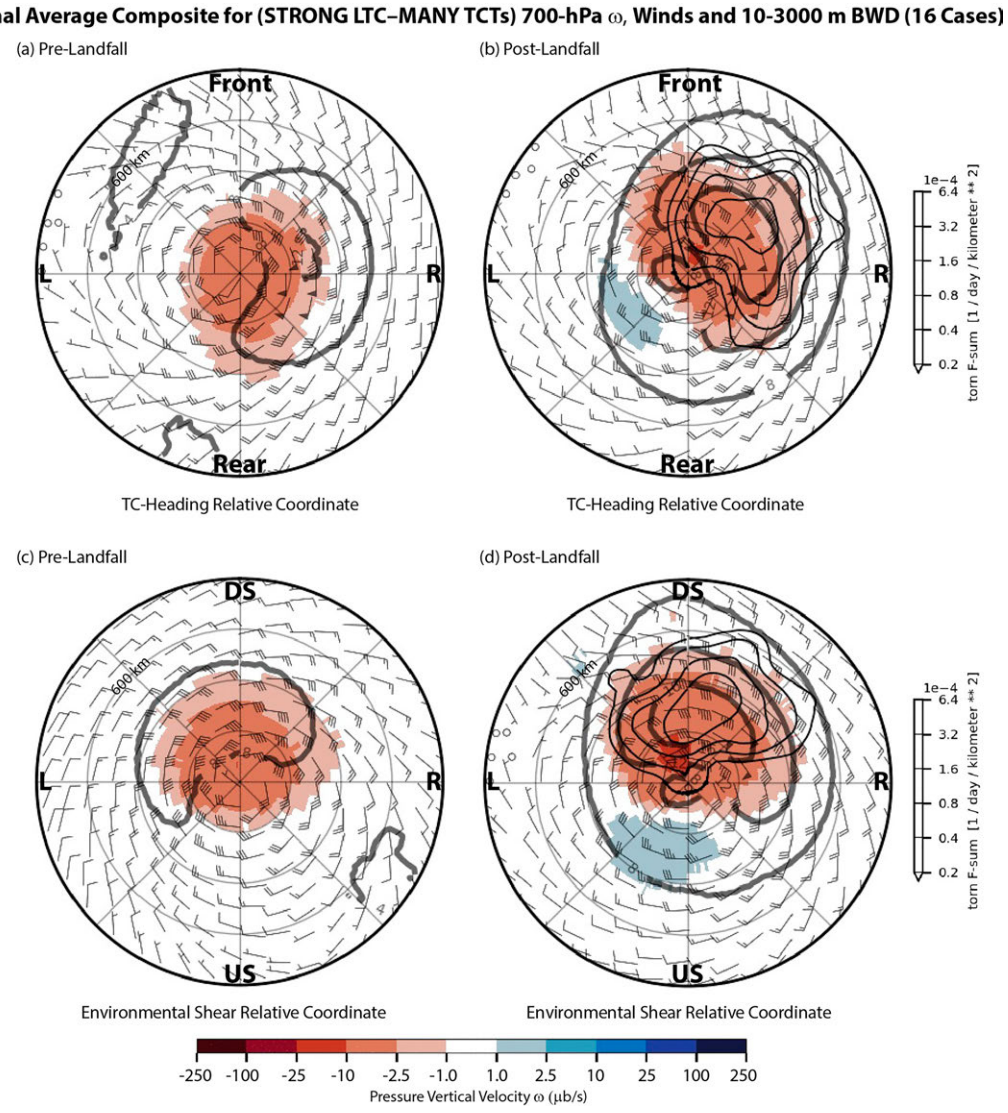

FIG. 13. Diurnally averaged F-sum tornado density (thin black contours, scale at far right), 700-hPa pressure vertical velocity (color shading) and winds (as in Fig. 7), and 10–3000-m BWD (thick gray contours; 8, 12, and 16 m s^{-1} contour values) for the 16-case STRONG LTC–MANY TCTs composite in (a),(b) TC-heading relative and (c),(d) 850–200-hPa environmental vertical shear relative coordinates (left) prior to and (right) following TC landfall.

MLCAPE values of 200–350 J kg^{-1} in the vicinity of the SRH03 maximum (cf. Figs. 14f and 15c).

Nearly all TCTs occurred within 600 km of LTC centers, and correlation coefficients R between F-sum TCT density fields and fields of NARR environmental predictors were calculated over the area defined by $r \leq 600$ km for the diurnally averaged 72-case ALL–CASES composite (Table 4). Thermodynamic parameters include surface-based CAPE (SBCAPE), MLCAPE, relative humidity at the first altitude where $T = 0°C$ ($RH_{0°C}$), and 850-hPa relative humidity (RH850). Kinematic parameters include wind speeds at 10 m (SPD10m), 700 hPa (SPD700), and 500 hPa (SPD500), 10-m–900-hPa (BWD900), 10-m–700-hPa (BWD700), and 10-m–500-hPa (BWD500) bulk wind difference magnitudes, and SRH03.

MLCAPE is spatially uncorrelated with TCT occurrence, but likely requires exceedance of at least some small threshold value to support TCTs. Consistent with Fig. 14, BWD500 is well correlated with the F-sum TCT density (Table 4). However, it is slightly outperformed by BWD700, which has correlation values comparable to SRH03 calculated through a similar layer. The correlation values differ quantitatively but are qualitatively similar for environmental parameters among the ground-relative, TC-heading relative, and environmental shear relative coordinate systems (Table 4).

Approximately 90% of TCTs are spawned from supercell thunderstorms within TC rainbands (Edwards et al. 2012). The supercell composite parameter (SCP), which has been employed in climatological studies of both Great Plains

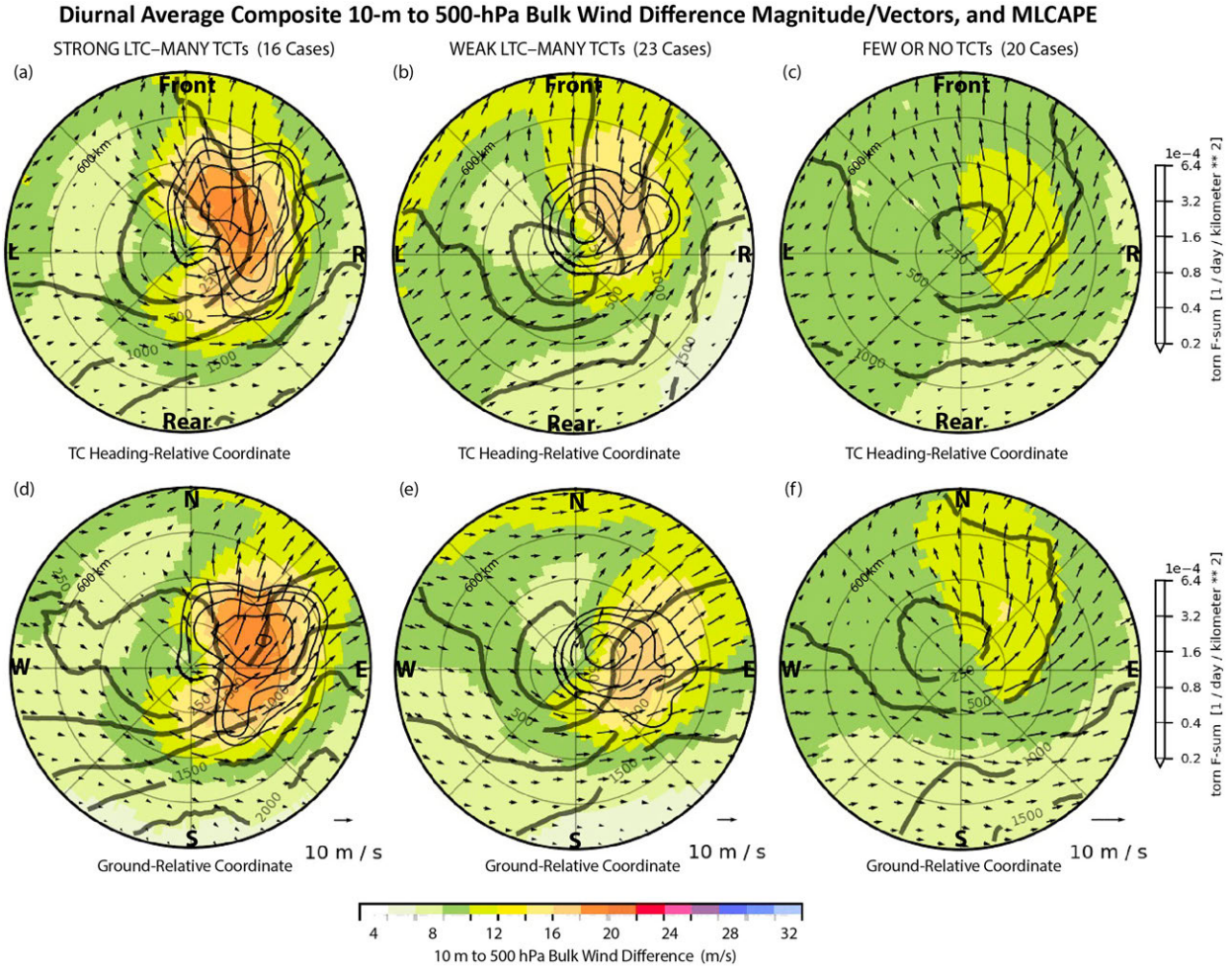

FIG. 14. Composite diurnally averaged F-sum tornado density (thin black contours, scale at far right), 10-m–500-hPa BWD magnitudes (color shading) and vectors, and MLCAPE (thick gray contours of 250, 500, 1000, 1500, and 2000 J kg^{-1}) in (top) TC-heading relative and (bottom) ground-relative coordinates for (a),(d) STRONG LTC–MANY TCTs; (b),(e) WEAK LTC–MANY TCTs; and (c),(f) FEW OR NO TCTs environment types (Table 1).

(e.g., Thompson et. 2003, 2007, 2012) and tropical cyclone (e.g., Edwards et al. 2012) tornadoes, is examined for the STRONG LTC–MANY TCTs, WEAK LTC–MANY TCTs, and FEW OR NO TCTs environments in Fig. 16.

Our SCP formulation is based on one used in the NOAA Storm Prediction Center (SPC) mesoanalysis, as defined by Gropp and Davenport (2018). However, the current formulation is defined as

$$\mathrm{SCP} = (\mathrm{SBCAPE}/1000\ \mathrm{J\ kg^{-1}}) \times (\mathrm{SRH03}/50\ \mathrm{m^2\ s^{-2}}) \times (\mathrm{BWD500}/20\ \mathrm{m\ s^{-1}}) \times (-40\ \mathrm{J\ kg^{-1}}/\mathrm{SBCIN}), \quad (2)$$

where, due to the limitations in the availability of NARR archive fields (section 2b), the surface-based convective inhibition (SBCIN) is substituted for the most unstable CIN (MUCIN) used in Gropp and Davenport (2018) but the ratio in the final term on the right of (2) is similarly set to 1.0 when $0 \leq \mathrm{SBCIN} < -40$. In similar fashion, surface-based CAPE (SBCAPE) is used in place of the most unstable CAPE (MUCAPE). These two changes are not expected to significantly alter results since surface parcels were typically found to have the largest θ_e and least CIN of any parcel in the vertical column. Also due to NARR data limitations, SRH03 is used instead of effective layer SRH ($\mathrm{SRH_{eff}}$) and BWD500 replaces the effective bulk wind difference (EBWD), where the effective layers in the original formulation are based on parcel CIN and CAPE constraints described in Thompson et al. (2007).

Maximum SCP values for the STRONG LTC–MANY TCTs (Figs. 16a,d) and WEAK LTC–MANY TCTs (Figs. 16b,e) TCT composites fall within the range for TC tornadoes reported by Edwards et al. (2012) based on sounding data. SCP discriminates well for the different TCT environment types. Maximum values are slightly greater in the STRONG LTC–MANY TCTs composite (Figs. 16a,d) than in the WEAK LTC–MANY TCTs composite (Figs. 16b,e) which also has large F-sum TCT densities. Particularly desirable is SCP's ability to discriminate between environments having many (Figs. 16b,e) or few or no (Figs. 16c,f) TCTs. Consistent with the daytime maximum in TCTs, SCP in

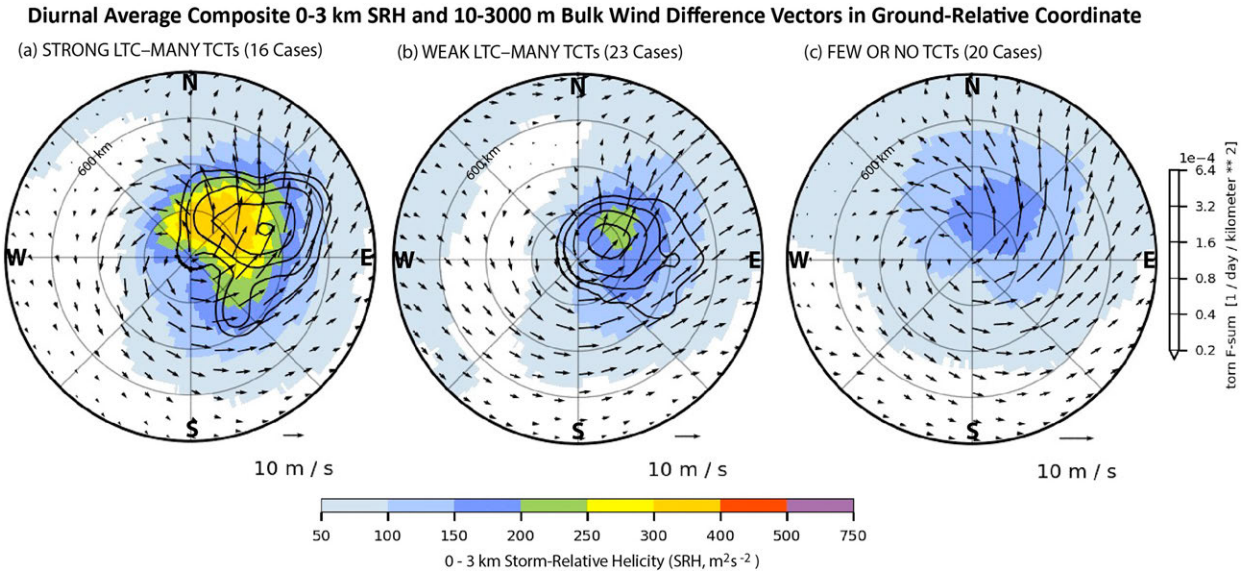

FIG. 15. Diurnally averaged F-sum tornado density (thin black contours, scale at far right), 0–3-km storm-relative helicity (color shading), and 10–3000-m BWD vectors in ground-relative coordinates for the (a) STRONG LTC–MANY TCTs, (b) WEAK LTC–MANY TCTs, and (c) FEW OR NO TCTs environment composites.

STRONG LTC–MANY TCTs and WEAK LTC–MANY TCTs environments is larger during the day (Figs. 16a,b) than at night (Figs. 16d,e). This diurnal variation is a beneficial aspect of SCP that is less evident with the BWDs and SRH03 (not shown). SCP maxima are situated near weak local maxima of TCT frequency at night in the southeast quadrant of the LTC (Figs. 16d,e), where MLCAPE is maximized. However, a limitation of SCP is its only moderate overall spatial correlation with F-sum TCT densities (Table 4, Fig. 16). This may result from too strong a dependence on the CAPE in (2), which is much smaller in most TCT environments than in typical continental tornado environments.

5. Comparison of inland TCT environments with other TCT environments

Typically, the production of TCTs decreases with distance inland from the coast (Hill et al. 1966; Schultz and Cecil 2009), though some inland environments remain favorable for TCTs. Therefore, it is instructive to compare such inland

TABLE 4. Correlation coefficients of selected NARR parameter fields with the F-sum TCT density (section 2c) field within 600 km of the LTC center for the diurnally averaged ALL–CASES composite of 72 cases comprising STRONG LTC–MANY TCTs, WEAK LTC–MANY TCTs, SOME TCTs, and FEW OR NO TCTs environment types. The R values in the second, third, and fourth columns are correlation coefficients computed in coordinates that are geographically fixed with north pointing up (Fig. 5d), tropical cyclone heading-relative with direction of the LTC motion pointing up (Fig. 5e), and environmental shear-relative with 850–200-hPa vertical shear direction pointing up (Fig. 5f), respectively.

NARR parameter	R (NARR, F-sum) for all cases (n = 72) in ground-relative coordinate	R (NARR, F-sum) for all cases (n = 72) in tropical cyclone heading relative coordinate	R (NARR, F-sum) for all cases (n = 72) in 850–200-hPa environmental shear relative coordinate
SRH03	0.80	0.83	0.76
BWD700	0.77	0.81	0.75
BWD500	0.74	0.79	0.73
BWD900	0.71	0.73	0.63
SPD500	0.68	0.70	0.64
SPD700	0.67	0.68	0.65
$RH_{0°C}$	0.62	0.61	0.56
SCP	0.54	0.74	0.69
RH850	0.53	0.42	0.51
SPD10m	0.49	0.48	0.59
SBCAPE	−0.08	−0.13	0.04
MLCAPE	−0.13	−0.20	−0.10

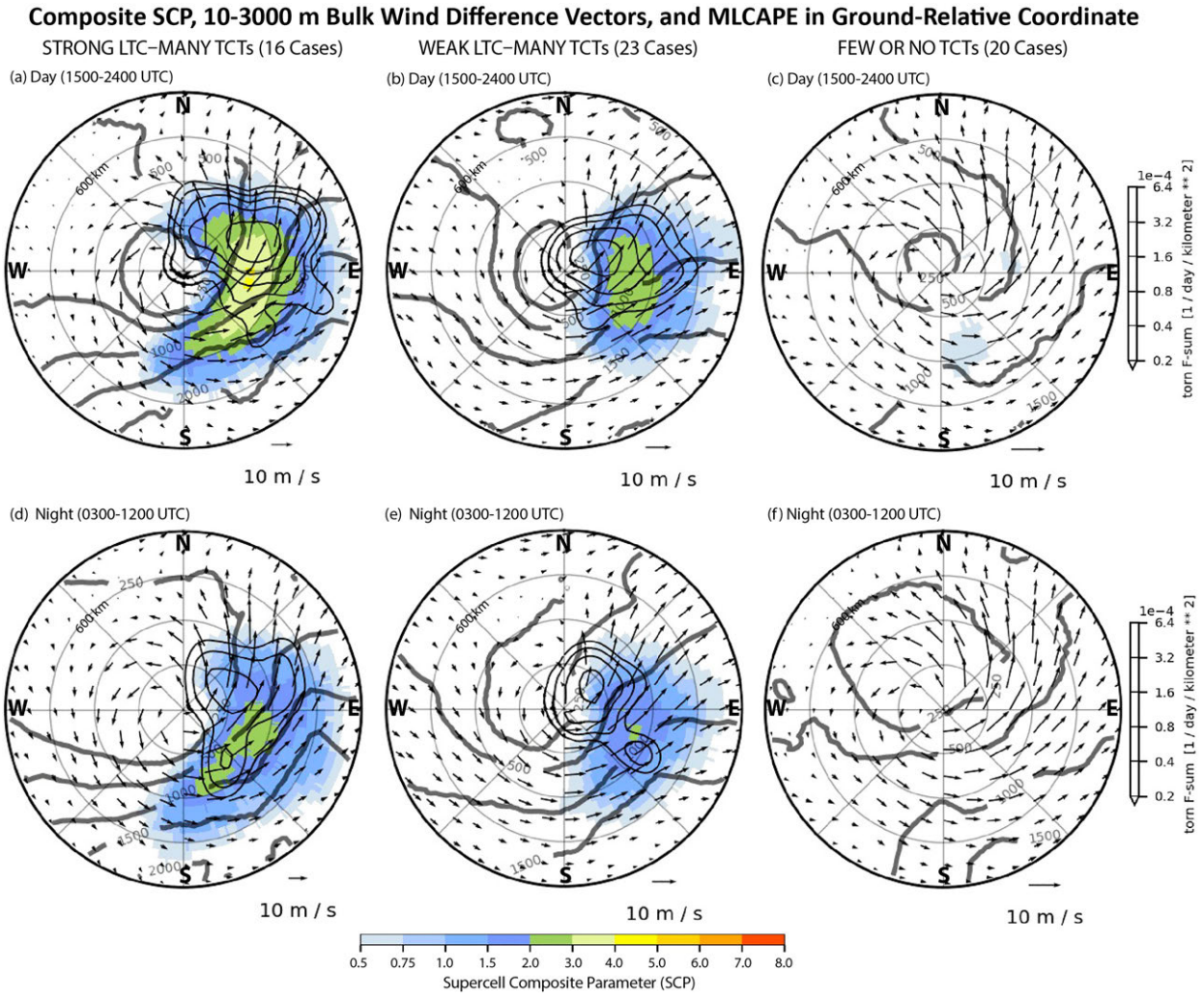

FIG. 16. Average supercell composite parameter (color shading), 10–3000-m BWD vectors, and MLCAPE (thick gray contours of 250, 500, 1000, 1500, and 2000 J kg^{-1}) for composites in ground-relative coordinates, which contain (top) 1500, 1800, 2100, and 0000 UTC NARR analyses with F-sum tornado density during 1330–0129 UTC (thin black contours, with scale at far right), and (bottom) 0300, 0600, 0900, and 1200 UTC NARR analyses with F-sum tornado density during 0130–1329 UTC (thin black contours, with scale at far right) overlaid for (a),(d) STRONG LTC–MANY TCTs; (b),(e) WEAK LTC–MANY TCTs; and (c),(f) FEW OR NO TCT environments (Table 1).

environments that support many TCTs with more generic TCT environments. This is accomplished by constructing an additional composite, INLAND, composed of LTC cases that produced five or more TCTs in a single diurnal cycle at least 24 h after TC landfall, and with the LTC center located 250 km or more from the coast, where this distance is defined by the nearest location along the coast from the inland TC center. As in previous 24-h composites (Figs. 1a–4a) we select the most tornadic diurnal cycle meeting the objective case selection criteria described above, which for the current environment type was usually the second or third diurnal cycle following landfall. The INLAND cases are drawn from the same 72 cases from which the previous composites have been constructed, but in most cases from later in the lifetime of the LTC.

The tracks of the 14 cases meeting the forestated INLAND selection criteria are shown in Fig. 17, with the 24-h periods used for the composite delineated by the solid portions of the LTC tracks. As noted for other composite TCT environment types, a large majority of the TCTs associated with the LTCs occur to the right of the storm track (Fig. 17) where, as before, the TCTs are color-coded to match that of the associated LTC. One notable difference from the previous LTC tracks based on either LTC strength or TCT frequencies (Figs. 1a–4a) is the more pronounced eastward path of the INLAND storm tracks (Fig. 17). This is indicative of the steering effect of stronger background westerlies when LTCs reach higher latitudes as they penetrate farther inland, which has been noted in previous studies (e.g., Verbout et al. 2007).

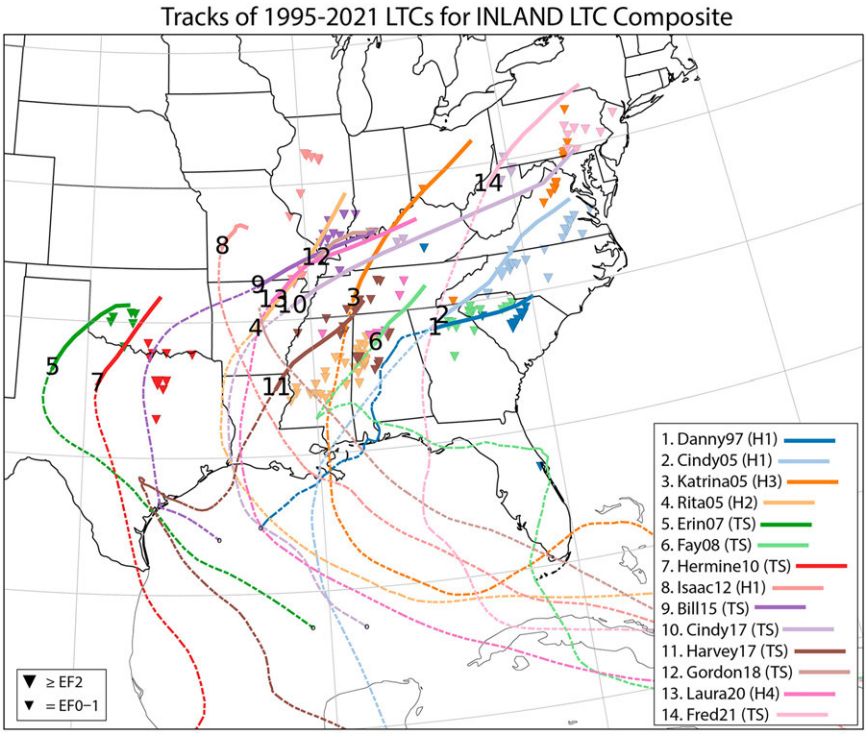

FIG. 17. As in Fig. 1a, but for the INLAND environment type.

It is anticipated that inland TCT outbreaks are favored for LTCs that are strong at landfall, but this idea is not supported by the percentages of LTC cases from the STRONG LTC–MANY TCTs (4 cases, 25%) and WEAK LTC–MANY TCTs (10 cases, 43%) composites that also met the qualifications for the INLAND composite (Fig. 17). This unexpected result could be influenced by the relatively small size of the INLAND composite (14 cases) but may also reflect the importance of the changing background environmental conditions as the TC moves inland.

The frequency distribution of TCTs for the 14 cases in the INLAND composite has a wide range (Fig. 18), but the mean of 13 TCTs within a 24-h period is comparable to the corresponding mean of 12 for the WEAK LTC–MANY TCTs composite (Table 1). Though also evident in other environment types associated with many TCTs (Table 1), the frequency distribution of TCTs within the INLAND composite (Fig. 18) illustrates an especially strong diurnal preference for daytime tornadoes.

The INLAND composite has stronger maximum 10-m–500-hPa BWD (Fig. 19a) than does the ALL–CASES composite (Fig. 19b). The stronger shear through the midtroposphere in inland environments, which is maximized in the eastern quadrants, also has a more westerly orientation (Fig. 19a) than for the ALL–CASES composite (Fig. 19b). Postlandfall environmental 850–200-hPa BWD for the INLAND composite is 14.38 m s^{-1} and is oriented along 257°. This environmental vertical shear is 4.46 m s^{-1} stronger than for the corresponding postlandfall ALL–CASES composite, is stronger than that of any of the individual TCT environment types (Table 3), and likely contributes to the particularly strong overall vertical shear in the eastern sector of the INLAND composite (Fig. 19a). Consistent with thermal wind considerations, the near westerly vertical shear along the east side of the LTC in the inland composite (Fig. 19a) is aligned along a roughly west–east-oriented baroclinic zone with a broad north–south temperature gradient (Fig. 20a).

The relatively strong vertical shear in the INLAND composite is consistent with the remnant TCs' encounter with enhanced environmental westerlies at more poleward latitudes. A well-developed midtropospheric mesoscale vertical motion couplet exists in INLAND cases (Fig. 20b), where ascent occurring on the eastern (downshear) side of the LTC (e.g., Molinari and Vollaro 2008; Schenkel et al. 2020, 2021) may be enhanced by the interaction of the remnant TC circulation with this baroclinic zone (Fig. 20a). Effects of large-scale frontal lifting are indicated by the concentrated zone of enhanced midtropospheric relative humidity (Fig. 20c) oriented along the baroclinic zone (Fig. 20a) that extends eastward beyond the outer TC circulation.

The midtropospheric relative humidity maximum occurs within the ascending portion of the vertical motion couplet and is located in the northeast quadrant close to the LTC center (Fig. 20c). There is a strong midtropospheric relative humidity minimum on the opposite side of the composite TC (Fig. 20c) slightly west of the maximum descent (Fig. 20b). The TCT maximum for the INLAND environment type occurs over a region with only modest MLCAPE of 250–500 J kg^{-1} (Fig. 19a). This seemingly suboptimal condition for TCTs is countered by

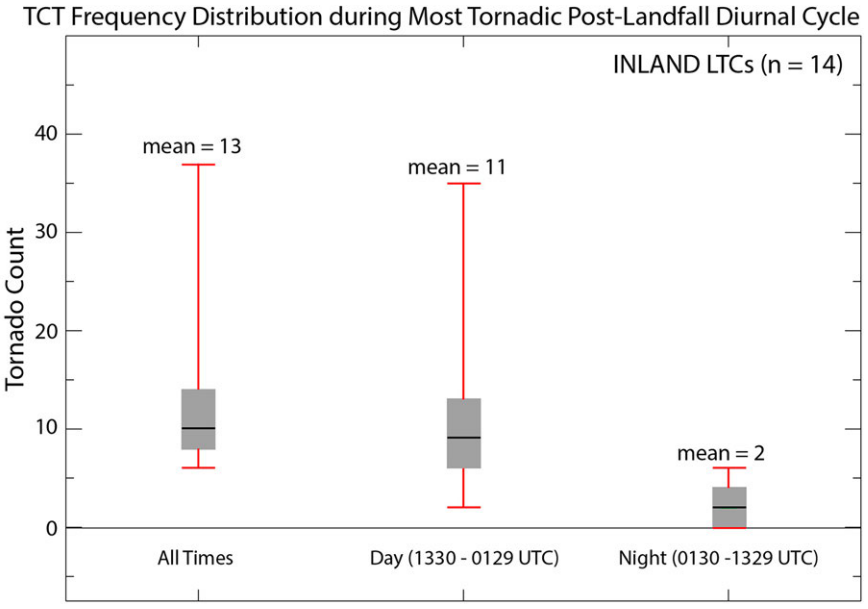

FIG. 18. Box-and-whisker plots for the frequency distribution of TCTs during the most tornadic 24-h periods occurring 24-h or more after TC landfall with LTC centers 250 km or more from the coast in the 14-case INLAND composite. The gray shaded rectangles comprise the 75th (top) and 25th (bottom) percentiles of the distribution, and the horizontal line indicates the median value. The red whiskers indicate the maximum (top) and minimum (bottom) of the distribution.

the collocated deep layer of large relative humidity (Fig. 20c), which has been shown more generally to support severe weather in high-shear low-CAPE environments (e.g., Sherburn and Parker 2014; Sherburn et al. 2016). In contrast to the ALL–CASES composite (Fig. 19b) there is an extensive southward extension of the TCT maximum toward larger MLCAPE values in the INLAND composite (Fig. 19a), which has considerably drier mid-tropospheric conditions (Fig. 20c).

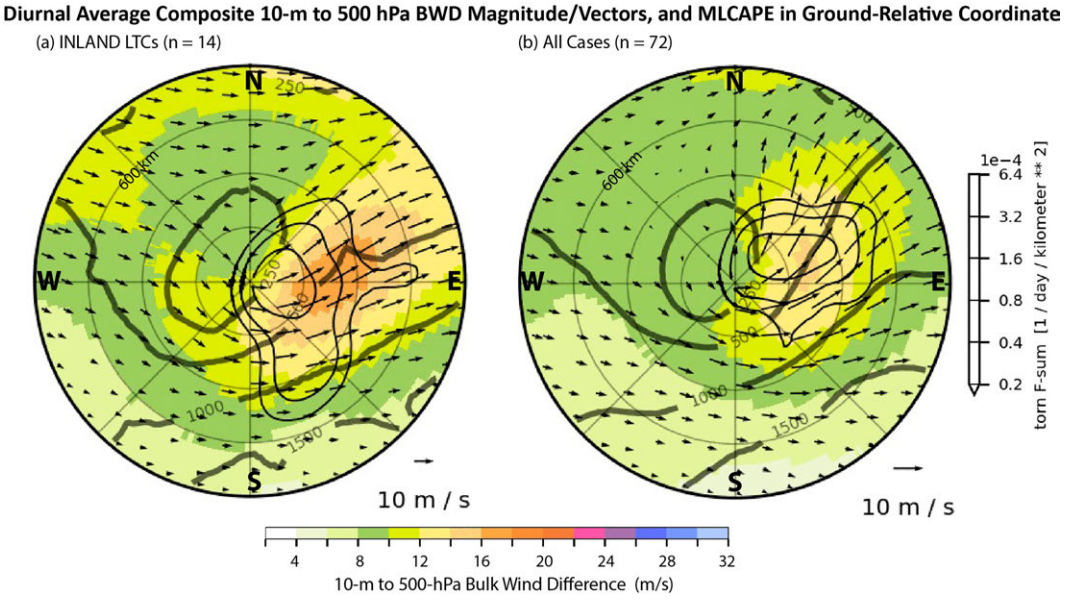

FIG. 19. Diurnally averaged F-sum tornado density (thin black contours, scale at far right), and NARR composite 10-m–500-hPa BWD magnitudes (color shading) and vectors, and surface-based CAPE (thick gray contours of 250, 500, 1000, and 1500 J kg^{-1}) in ground-relative coordinates for the (a) $n = 14$ INLAND and (b) $n = 72$ ALL–CASES composites.

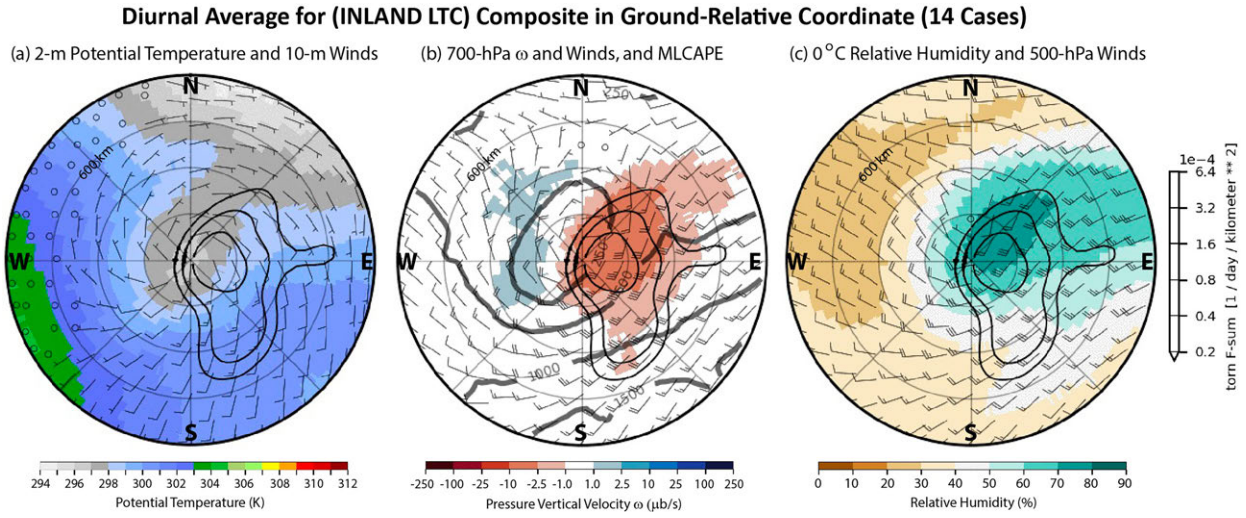

FIG. 20. Diurnally averaged F-sum tornado density (thin black contours, scale at far right), and NARR 14-case composites of (a) 10-m winds and 2-m potential temperature (color shading), (b) 700-hPa winds and pressure vertical velocity (color shading), and MLCAPE (thick gray contours of 250, 500, 1000, and 1500 J kg^{-1}), and (c) 500-hPa winds and relative humidity at 0°C (color shading) for INLAND TCT environments in ground-relative coordinates. The winds in each part are plotted as in Fig. 7.

6. Summary

Mesoscale environments of tropical cyclone tornadoes (TCTs) have been examined using 27 years (1995–2021) of reanalysis output for both strong and weak-to-moderate landfalling tropical cyclones (LTCs), where strong and weak to moderate connote category-2 or greater hurricanes, and tropical storms/category-1 hurricanes at landfall, respectively. From these data, multicase composites were constructed for different TCT environment types including 1) strong landfalling tropical cyclones (LTCs) with many TCTs, 2) weak-to-moderate LTCs with many TCTs, 3) LTCs with an intermediate TCT frequency 4) LTCs with few or no TCTs, and 5) environments with TCTs occurring ≥250 km from the coast, and at least one diurnal cycle after TC landfall. In these composites, averages of environmental predictors from the reanalyses are examined relative to the spatial distribution of TCTs. The composite approach using reanalyses augments past studies containing more cases (which are often sounding-based) by providing forecasters with information on spatial relationships between mesoscale forcing and TCT occurrence for a greater number of distinctly different TCT environments.

We examined the diurnal cycle of the TCT environment for a more generic LTC using a 72-case composite constructed from an average of the type 1, 2, 3, and 4 composites. As found in numerous previous studies, TCTs are most common in the afternoon close to where the lower-tropospheric (e.g., 0–3 km AGL) vertical shear is maximized 200–400 km northeast of the LTC center. Across the LTC circulation, relatively minor diurnal variations in the vertical shear magnitude occur. However, modest local increases in low-level vertical shear at night in the southeast quadrant of the LTC appears associated with a nocturnal southward extension of the envelope of TCT occurrence toward locations where MLCAPE remains near or above 500 J kg^{-1}.

A 700-hPa mesoscale vertical motion couplet becomes increasingly prominent after TC landfall. This occurs in response to increasing regional-scale vertical shear influenced by frictionally induced differential slowing of the winds in the vertical over land, and is likely augmented by greater deep (850–200 hPa) environmental vertical shear at inland locations. The stronger mesoscale ascent in the downshear direction after TC landfall may help reinforce the pronounced daytime TCT maximum by helping to provide better forcing for deep convection near locations of maximum regional-scale lower-tropospheric vertical shear.

The strongest LTCs at landfall were associated with the most TCTs. However, an important objective of the current study that has forecast implications, was to assess factors influencing why some weaker LTCs produce many TCTs but others produce few or none. Differences in TCT frequencies in composites containing weaker landfalling TCs are influenced by both differences in the 10-m–700-hPa bulk wind difference (BWD700) and MLCAPE in their northeast and southeast quadrants. Despite having similar average 10-m TC windspeeds at landfall, environments with many TCTs had BWD700 that was 4 m s^{-1} (~20%) greater and MLCAPE that was ~500 J kg^{-1} greater in the NE quadrant of the LTC than in environments that produced few or no TCTs. The differences in the strength of the overall BWD700 was likely influenced by much larger postlandfall increases in the environmental vertical shear near weak LTCs that had many TCTs than in those which had few or no TCTs.

Spatial correlations between environmental predictor fields derived from the reanalyses and a TCT density field based on the F sum (McCaul 1991) were evaluated within the range of $r \leq 600$ km from the LTC center for the 72-case merged composite of type 1, 2, 3, and 4 TCT environments. The severe weather predictors of BWD700, and 0–3-km cell-relative

helicity (SRH03) were among the best of all tested predictors, with correlation coefficients of $R \approx 0.8$, which were qualitatively similar in ground-relative, TC-heading relative, and 850–200-hPa environmental shear-relative coordinate systems.

Since TCTs are often associated with supercells in outer LTC rainbands, we similarly computed the correlation with TCT density field of a slightly modified version of the supercell composite parameter (SCP). Spatial correlations were less than those for BWD700 and SRH03, but SCP combines thermodynamic with kinematic information resulting in a strong diurnal cycle consistent with that of the TCT density, which does not occur for BWD700 and SRH03.

The composite of inland TCT environments with many TCTs had a broad north–south oriented surface temperature gradient, and stronger associated westerly vertical shear than for other composites. A particularly well-defined mesoscale midtropospheric vertical motion couplet is consistent with the stronger vertical shear. In this composite, the ascending motion on the east side of the LTC is likely enhanced by TC-induced flow across the baroclinic zone and helps support deep convection in strong vertical shear, thereby favoring TCTs in this location.

Acknowledgments. The authors have benefitted from conversations with Ben Schenkel (University of Oklahoma), Morris Weisman, Rosimar Rios-Berrios, and Chris Davis (each of NCAR). The comments and suggestions of three anonymous reviewers led to important clarifications and improvements in the paper. This research is supported by NOAA Award NA19OAR4590215 as part of the Verification of Rotation in Tornadoes (VORTEX-SE) Research Program, and by National Science Foundation funds for the U. S. Weather Research Program (USWRP), which supports NCAR's Short-Term Explicit Prediction (STEP) program. The National Center for Atmospheric Research is sponsored by the National Science Foundation.

Data availability statement. The tropical cyclones selected for the analyses presented in this paper were identified from the NHC archive (https://www.nhc.noaa.gov/data/#hurdat). TCT locations and intensities were obtained from the TCTOR dataset (https://www.spc.noaa.gov/publications/edwards/tctor.xls). The TC positions used in the composites were obtained from the IBTrACS dataset (https://www.ncei.noaa.gov/data/international-best-track-archive-for-climate-stewardship-ibtracs/v04r00/access/netcdf/), and the NARR reanalyses supplying environmental conditions from which composites were generated are found at https://psl.noaa.gov/gridded/data.narr.html.

APPENDIX

NWS Soundings Used in Comparisons with NARR Analyses

In Table A1 we list the NWS soundings used to assess the realism of the NARR analysis TCT environmental predictors reported in section 2b.

TABLE A1. National Weather Service (NWS) soundings to the right and left of LTC tracks that are used for comparisons with collocated NARR output (Figs. 5 and 6, Table 2) for the 72 cases used in the ALL-CASES composite TCT environment.

TCT environment type	TC case (name/yy)	Time (UTC) + date	Sounding right of TC heading (°N lat, °W lon)	Distance (km) from TC center	Time (UTC) + date	Sounding left of TC heading (°N lat, °W lon)	Distance (km) from TC center
SOME TCTs	Allison95	1200 UTC 5 Jun	JAX (30.50, 81.70)	306	0000 UTC 6 Jun	FFC (33.36, 84.56)	239
SOME TCTs	Dean95	0000 UTC 31 Jul	LCH (30.11, 93.21)	213	0000 UTC 31 Jul	CRP (27.76, 97.50)	281
WEAK LTC–MANY TCTs	Erin95	0000 UTC 3 Aug	TLH (30.45, 84.30)	188	1200 UTC 2 Aug	MFL (25.75, 80.38)	312
FEW OR NO TCTs	Jerry95	1200 UTC 24 Aug	FFC (33.36, 84.56)	234	1200 UTC 24 Aug	TBW (27.70, 82.40)	98
STRONG LTC–MANY TCTs	Opal95	1800 UTC 4 Oct	TLH (30.45, 84.30)	366		Unavailable	
FEW OR NO TCTs	Fran96	1200 UTC 6 Sep	WAL (37.93, 75.48)	340	0000 UTC 6 Sep	CHS (32.90, 80.03)	208
WEAK LTC–MANY TCTs	Danny97	0000 UTC 24 Jul	CHS (32.90, 80.03)	276	0000 UTC 24 Jul	RNK (37.20, 80.41)	359
FEW OR NO TCTs	Charley98	1200 UTC 22 Aug	LCH (30.11, 93.21)	476	0000 UTC 22 Aug	BRO (25.91, 97.41)	221
WEAK LTC–MANY TCTs	Earl98	1200 UTC 3 Sep	JAX (30.50, 81.70)	237	0000 UTC 3 Sep	BMX (33.16, 86.76)	418
WEAK LTC–MANY TCTs	Frances98	0000 UTC 12 Sep	LCH (30.11, 93.21)	368	0000 UTC 12 Sep	BRO (25.91, 97.41)	380
STRONG LTC–MANY TCTs	Georges98	0000 UTC 29 Sep	TLH (30.45, 84.30)	450	0000 UTC 29 Sep	LCH (30.11, 93.21)	408
SOME TCTs	Bret99	0000 UTC 23 Aug	CRP (27.76, 97.50)	96	1800 UTC 22 Aug	BRO (25.91, 97.41)	98
FEW OR NO TCTs	Dennis99	0000 UTC 5 Sep	WAL (37.93, 75.48)	347	0000 UTC 5 Sep	GSO (36.08, 79.95)	309
WEAK LTC–MANY TCTs	Helene00	0000 UTC 23 Sep	CHS (32.90, 80.03)	324	1200 UTC 22 Sep	JAN (32.31, 90.08)	387
WEAK LTC–MANY TCTs	Allison01	0000 UTC 13 Jun	CHS (32.90, 80.03)	241	0000 UTC 13 Jun	GSO (36.08, 79.95)	411
SOME TCTs	Barry01	0000 UTC 7 Aug	BMX (33.16, 86.76)	163	1800 UTC 6 Aug	JAN (32.31, 90.08)	227
WEAK LTC–MANY TCTs	Gabrielle01	1800 UTC 14 Sep	XMR (28.46, 80.55)	133	1800 UTC 14 Sep	TLH (30.45, 84.30)	365
FEW OR NO TCTs	Bertha02	1800 UTC 5 Aug	JAN (32.31, 90.08)	164	0000 UTC 6 Aug	LCH (30.11, 90.08)	229
FEW OR NO TCTs	Edouard02	1200 UTC 5 Sep	JAX (30.50, 81.70)	190	1200 UTC 5 Sep	TBW (27.70, 82.40)	133
WEAK LTC–MANY TCTs	Fay02	1200 UTC 7 Sep	LCH (30.11, 93.21)	374	0600 UTC 7 Sep	BRO (25.91, 97.41)	302
FEW OR NO TCTs	Hanna02	1200 UTC 14 Sep	BMX (33.16, 86.76)	401	1200 UTC 14 Sep	LCH (30.11, 93.21)	425
WEAK LTC–MANY TCTs	Lili02	1800 UTC 3 Oct	JAN (32.31, 90.08)	298		Unavailable	
WEAK LTC–MANY TCTs	Bill03	0000 UTC 2 Jul	FFC (33.36, 84.56)	157	0000 UTC 2 Jul	LZK (34.83, 92.27)	580
FEW OR NO TCTs	Claudette03	0000 UTC 16 Jul	CRP (27.76, 97.50)	107	0000 UTC 16 Jul	DRT (29.36, 100.91)	399
FEW OR NO TCTs	Grace03	0000 UTC 1 Sep	LCH (30.11, 93.21)	318	0000 UTC 1 Sep	CRP (27.76, 97.50)	365
FEW OR NO TCTs	Isabel03	0000 UTC 19 Sep	WAL (37.79, 75.48)	239	0000 UTC 19 Sep	CHS (32.90, 80.03)	473
WEAK LTC–MANY TCTs	Gaston04	1200 UTC 30 Aug	WAL (37.79, 75.48)	386	0000 UTC 31 Aug	GSO (36.08, 79.95)	324
STRONG LTC–MANY TCTs	Frances04	0000 UTC 8 Sep	GSO (36.08, 79.95)	526	0000 UTC 8 Sep	JAN (32.31, 90.08)	517

TABLE A1. (*Continued*)

TCT environment type	TC case (name/yy)	Time (UTC) + date	Sounding right of TC heading (°N lat, °W lon)	Distance (km) from TC center	Time (UTC) + date	Sounding left of TC heading (°N lat, °W lon)	Distance (km) from TC center
STRONG LTC–MANY TCTs	Ivan04	1200 UTC 16 Sep	FFC (33.36, 84.56)	367	1800 UTC 16 Sep	JAN (32.31, 90.08)	252
STRONG LTC–MANY TCTs	Jeanne04	0000 UTC 28 Sep	MHX (34.78, 76.88)	608	0000 UTC 28 Sep	BMX (33.16, 86.76)	331
FEW OR NO TCTs	Matthew04	1200 UTC 10 Oct	LIX (30.33, 89.77)	150	1200 UTC 10 Oct	LCH (30.11, 93.21)	237
FEW OR NO TCTs	Arlene05	0000 UTC 12 Jun	FFC (36.36, 84.57)	359	0000 UTC 12 Jun	LCH (30.11, 93.21)	555
WEAK LTC–MANY TCTs	Cindy05		Unavailable		0000 UTC 7 Jul	JAN (32.31, 90.08)	271
STRONG LTC–MANY TCTs	Katrina05	0000 UTC 30 Aug	FFC (33.36, 84.57)	432	0000 UTC 30 Aug	SHV (32.46, 93.78)	439
STRONG LTC–MANY TCTs	Rita05	0000 UTC 25 Sep	JAN (32.31, 90.08)	370	0000 UTC 25 Sep	FWD (32.83, 97.30)	275
FEW OR NO TCTs	Tammy05	0000 UTC 6 Oct	CHS (32.90, 80.03)	305	1200 UTC 6 Oct	TLH (30.45, 84.30)	153
WEAK LTC–MANY TCTs	Alberto06	0000 UTC 14 Jun	CHS (32.90, 80.03)	316	0000 UTC 14 Jun	BMX (33.16, 86.76)	426
SOME TCTs	Ernesto06	1200 UTC 1 Sep	MHX (34.78, 76.88)	107	1200 UTC 1 Sep	GSO (36.08, 79.95)	214
SOME TCTs	Erin07	0000 UTC 19 Aug	OUN (35.18, 94.77)	246	0000 UTC 19 Aug	AMA (35.23, 101.70)	153
FEW OR NO TCTs	Humberto07	0000 UTC 14 Sep	LIX (30.33, 89.77)	285	0000 UTC 14 Sep	FWD (32.83, 97.30)	664
SOME TCTs	Dolly08	0000 UTC 24 Jul	CRP (27.76, 97.50)	143		Unavailable	
FEW OR NO TCTs	Edouard08	0000 UTC 6 Aug	LCH (30.11, 93.21)	245	0000 UTC 6 Aug	CRP (27.76, 97.50)	381
STRONG LTC–MANY TCTs	Gustav08	0000 UTC 2 Sep	JAN (32.31, 90.08)	276	0000 UTC 2 Sep	CRP (27.76, 97.50)	601
STRONG LTC–MANY TCTs	Ike08	0000 UTC 14 Sep	LZK (34.83, 92.27)	284	0000 UTC 14 Sep	FWD (32.83, 97.30)	235
WEAK LTC–MANY TCTs	Hermine10	0900 UTC 9 Sep	FWD (32.83, 97.30)	215	1800 UTC 14 Sep	AMA (35.23, 101.70)	351
WEAK LTC–MANY TCTs	Lee11	0000 UTC 5 Sep	BMX (33.16, 86.76)	551	0000 UTC 5 Sep	LCH (30.11, 83.21)	158
SOME LTCs	Beryl12	0000 UTC 29 May	JAX (30.50, 81.70)	144	1200 UTC 29 May	TLH (30.45, 84.30)	156
FEW OR NO TCTs	Sandy12	0000 UTC 30 Oct	OKX (40.86, 72.86)	206	0000 UTC 30 Oct	IAD (38.98, 77.46)	261
FEW OR NO TCTs	Ana15	1200 UTC 10 May	MHX (34.78, 76.88)	202	0000 UTC 11 May	CHS (32.90, 80.03)	245
WEAK LTC–MANY TCTs	Bill15	0000 UTC 20 Jun	BNA (36.25, 86.57)	282	0000 UTC 20 Jun	ILX (40.15, 89.33)	306
WEAK LTC–MANY TCTs	Hermine16	0000 UTC 2 Sep	XMR (28.46, 80.55)	419	0000 UTC 2 Sep	JAN (32.31, 90.08)	625
WEAK LTC–MANY TCTs	Cindy17	0000 UTC 24 Jun	BNA (36.25, 86.57)	251	1200 UTC 23 Jun	ILX (40.15, 89.33)	533
STRONG LTC–MANY TCTs	Harvey17	0000 UTC 26 Aug	LCH (30.11, 93.21)	433	1800 UTC 26 Aug	BRO (25.91, 97.41)	344
STRONG LTC–MANY TCTs	Irma17	0000 UTC 11 Sep	JAX (30.50, 81.70)	411	1200 UTC 11 Sep	BMX (33.16, 86.76)	552
WEAK LTC–MANY TCTs	Nate17	0000 UTC 9 Oct	GSO (36.08, 79.95)	516	0000 UTC 9 Oct	BNA (36.25, 86.57)	78
SOME TCTs	Alberto18	0000 UTC 31 May	ILN (39.41, 83.81)	297	0000 UTC 31 May	ILX (40.15, 89.33)	318

TABLE A1. (*Continued*)

TCT environment type	TC case (name/yy)	Time (UTC) + date	Sounding right of TC heading (°N lat, °W lon)	Distance (km) from TC center	Time (UTC) + date	Sounding left of TC heading (°N lat, °W lon)	Distance (km) from TC center
SOME TCTs	Gordon18	0000 UTC 6 Sep	BMX (33.16, 86.76)	386	0000 UTC 6 Sep	LZK (34.83, 92.27)	240
STRONG LTC–MANY TCTs	Florence18	0000 UTC 17 Sep	GSO (36.08, 79.95)	236	0000 UTC 17 Sep	FFC (33.36, 84.57)	284
STRONG LTC–MANY TCTs	Michael18	0000 UTC 11 Oct	JAX (30.50, 81.70)	289	0000 UTC 11 Oct	LIX (30.34, 89.83)	524
FEW OR NO TCTs	Barry19	0000 UTC 14 Jul	LIX (30.34, 89.83)	285	0000 UTC 14 Jul	CRP (27.76, 97.50)	543
SOME TCTs	Nestor19	0000 UTC 20 Oct	JAX (30.50, 81.70)	251	0000 UTC 20 Oct	BMX (33.16, 86.76)	325
FEW OR NO TCTs	Bertha20	0000 UTC 28 May	MHX (34.78, 76.88)	349		Unavailable	
SOME TCTs	Hanna20	0000 UTC 26 Jul	CRP (27.76, 97.50)	118	1800 UTC 25 Jul	BRO (25.91, 97.41)	126
WEAK LTC–MANY TCTs	Isaias20	0000 UTC 4 Aug	MHX (34.78, 76.88)	301	0000 UTC 4 Aug	GSO (36.08, 79.95)	373
STRONG LTC–MANY TCTs	Laura20	1800 UTC 27 Aug	JAN (32.31, 90.08)	270	0000 UTC 28 Aug	FWD (32.83, 97.30)	477
STRONG LTC–MANY TCTs	Sally20	1200 UTC 27 Sep	CHS (32.90, 80.03)	485	0000 UTC 28 Sep	FFC (33.36, 84.57)	214
WEAK LTC–MANY TCTs	Delta20	1200 UTC 10 Oct	BMX (33.16, 86.76)	440	1200 UTC 10 Oct	LZK (34.83, 92.27)	272
FEW OR NO TCTs	Zeta20	0000 UTC 29 Oct	TLH (30.45, 84.30)	538	0000 UTC 29 Oct	LCH (30.11, 93.21)	318
SOME TCTs	Claudette21	1200 UTC 19 Jun	TLH (30.45, 84.30)	537	0000 UTC 20 Jun	JAN (32.31, 90.08)	214
WEAK LTC–MANY TCTs	Elsa21	0000 UTC 8 Jul	CHS (32.90, 80.03)	296	0000 UTC 8 Jul	FFC (33.36, 84.56)	271
WEAK LTC–MANY TCTs	Fred21	0000 UTC 18 Aug	CHS (32.90, 80.03)	467	0000 UTC 18 Aug	BNA (36.25, 86.57)	270
STRONG LTC–MANY TCTs	Ida21	0000 UTC 1 Sep	FFC (33.36, 84.56)	284		Unavailable	

REFERENCES

Baker, A. K., M. D. Parker, and M. D. Eastin, 2009: Environmental ingredients for supercells and tornadoes within Hurricane Ivan. *Wea. Forecasting*, **24**, 223–244, https://doi.org/10.1175/2008WAF2222146.1.

Bunkers, M. J., B. A. Klimowski, J. W. Zeitler, R. L. Thompson, and M. L. Weisman, 2000: Predicting supercell motion using a new hodograph technique. *Wea. Forecasting*, **15**, 61–79, https://doi.org/10.1175/1520-0434(2000)015<0061:PSMUAN>2.0.CO;2.

Coffer, B. E., M. Taszarek, and M. D. Parker, 2020: Near ground wind profiles of tornadic and nontornadic environments in the United States and Europe from ERA5 reanalyses. *Wea. Forecasting*, **35**, 2621–2638, https://doi.org/10.1175/WAF-D-20-0153.1.

Coniglio, M. C., and R. E. Jewell, 2022: SPC mesoscale analysis compared to field project soundings: Implications for supercell environment studies. *Mon. Wea. Rev.*, **150**, 567–588, https://doi.org/10.1175/MWR-D-21-0222.1.

Davies-Jones, R. P., D. W. Burgess, and M. Foster, 1990: Test of helicity as a tornado forecast parameter. Preprints, *16th Conf. on Severe Local Storms*, Kananaskis Park, AB, Canada, Amer. Meteor. Soc., 588–592.

Davis, C., C. Snyder, and A. C. Didlake Jr., 2008: A vortex-based perspective of eastern Pacific tropical cyclone formation. *Mon. Wea. Rev.*, **136**, 2461–2477, https://doi.org/10.1175/2007MWR2317.1.

Eastin, M. D., and M. C. Link, 2009: Miniature supercells in an offshore outer rainband of Hurricane Ivan (2004). *Mon. Wea. Rev.*, **137**, 2081–2104, https://doi.org/10.1175/2009MWR2753.1.

——, B. M. Hays, and M. C. Link, 2014: A tropical cyclone tornado parameter for use in situational awareness forecasting. *31st Conf. on Hurricanes and Tropical Meteorology*, San Diego, CA, Amer. Meteor. Soc., 176, https://ams.confex.com/ams/31Hurr/webprogram/Paper243962.html.

Edwards, R., 2010: Tropical cyclone tornado records for the modernized National Weather Service era. *25th Conf. on Severe Local Storms*, Denver, CO, Amer. Meteor. Soc., P3.1, https://ams.confex.com/ams/25SLS/techprogram/paper_175269.htm.

——, 2012: Tropical cyclone tornadoes: A review of knowledge in research and prediction. *Electron. J. Severe Storms Meteor.*, **7** (6), https://doi.org/10.55599/ejssm.v7i6.42.

——, and R. M. Mosier, 2022: Over a quarter century of TCTOR: Tropical cyclone tornadoes in the WSR-88D era. *30th Conf. on Severe Local Storms*, Santa Fe, NM, Amer. Meteor. Soc., P171, https://www.spc.noaa.gov/publications/edwards/27yr-sls.pdf.

——, A. R. Dean, R. L. Thompson, and B. T. Smith, 2012: Convective modes for significant severe thunderstorms in the contiguous United States. Part III: Tropical cyclone tornadoes. *Wea. Forecasting*, **27**, 1507–1519, https://doi.org/10.1175/WAF-D-11-00117.1.

Galarneau, T. J., Jr., and C. A. Davis, 2013: Diagnosing forecast errors in tropical cyclone motion. *Mon. Wea. Rev.*, **141**, 405–430, https://doi.org/10.1175/MWR-D-12-00071.1.

Gentry, R. C., 1983: Genesis of tornadoes associated with hurricanes. *Mon. Wea. Rev.*, **111**, 1793–1805, https://doi.org/10.1175/1520-0493(1983)111<1793:GOTAWH>2.0.CO;2.

Gropp, M. E., and C. E. Davenport, 2018: The impact of the nocturnal transition on the lifetime and evolution of supercell thunderstorms in the Great Plains. *Wea. Forecasting*, **33**, 1045–1061, https://doi.org/10.1175/WAF-D-17-0150.1.

Hill, E. L., W. Malkin, and W. A. Schulz Jr., 1966: Tornadoes associated with cyclones of tropical origin-practical features. *J. Appl. Meteor.*, **5**, 745–763, https://doi.org/10.1175/1520-0450(1966)005<0745:TAWCOT>2.0.CO;2.

Knapp, K. R., M. C. Kruk, D. H. Levinson, H. J. Diamond, and C. J. Neumann, 2010: The International Best Track Archive for Climate Stewardship (IBTrACS): Unifying tropical cyclone data. *Bull. Amer. Meteor. Soc.*, **91**, 363–376, https://doi.org/10.1175/2009BAMS2755.1.

——, H. J. Diamond, J. P. Kossin, M. C. Kruk, and C. J. Schreck III, 2018: International Best Track Archive for Climate Stewardship (IBTrACS) project, version 4. NOAA NCEI, accessed 13 March 2020, https://doi.org/10.25921/82ty-9e16.

Mashiko, W., H. Niino, and T. Kato, 2009: Numerical simulation of tornadogenesis in an outer-rainband minisupercell of Typhoon Shanshan on 17 September 2006. *Mon. Wea. Rev.*, **137**, 4238–4260, https://doi.org/10.1175/2009MWR2959.1.

McCaul, E. W., Jr., 1991: Buoyancy and shear characteristics of hurricane-tornado environments. *Mon. Wea. Rev.*, **119**, 1954–1978, https://doi.org/10.1175/1520-0493(1991)119<1954:BASCOH>2.0.CO;2.

——, and M. L. Weisman, 1996: Simulations of shallow supercell storms in landfalling hurricane environments. *Mon. Wea. Rev.*, **124**, 408–429, https://doi.org/10.1175/1520-0493(1996)124<0408:SOSSSI>2.0.CO;2.

——, and ——, 2001: The sensitivity of simulated supercell structure and intensity to variations in the shapes of environmental buoyancy and shear profiles. *Mon. Wea. Rev.*, **129**, 664–687, https://doi.org/10.1175/1520-0493(2001)129<0664:TSOSSS>2.0.CO;2.

——, and C. Cohen, 2002: The impact of simulated storm structure and intensity on variations in the mixed layer and moist layer depths. *Mon. Wea. Rev.*, **130**, 1722–1748, https://doi.org/10.1175/1520-0493(2002)130<1722:TIOSSS>2.0.CO;2.

Mesinger, F., and Coauthors, 2006: North American Regional Reanalysis. *Bull. Amer. Meteor. Soc.*, **87**, 343–360, https://doi.org/10.1175/BAMS-87-3-343.

Molinari, J., and D. Vollaro, 2008: Extreme helicity and intense convective towers in Hurricane Bonnie. *Mon. Wea. Rev.*, **136**, 4355–4372, https://doi.org/10.1175/2008MWR2423.1.

Moore, T. W., and R. W. Dixon, 2015: Patterns in 500 hPa geopotential height associated with temporal clusters of tropical cyclone tornadoes. *Meteor. Appl.*, **22**, 314–322, https://doi.org/10.1002/met.1456.

Morin, M. J., and M. D. Parker, 2011: A numerical investigation of supercells in landfalling tropical cyclones. *Geophys. Res. Lett.*, **38**, L10801, https://doi.org/10.1029/2011GL047448.

Novlan, D. J., and W. M. Gray, 1974: Hurricane-spawned tornadoes. *Mon. Wea. Rev.*, **102**, 476–488, https://doi.org/10.1175/1520-0493(1974)102<0476:HST>2.0.CO;2.

Nowotarski, C. J., J. Spotts, R. Edwards, S. Overpeck, and G. R. Woodall, 2021: Tornadoes in Hurricane Harvey. *Wea. Forecasting*, **36**, 1589–1609, https://doi.org/10.1175/WAF-D-20-0196.1.

Rappaport, E. N., 2014: Fatalities in the United States from Atlantic tropical cyclones. *Bull. Amer. Meteor. Soc.*, **95**, 341–346, https://doi.org/10.1175/BAMS-D-12-00074.1.

Rasmussen, E. N., and D. O. Blanchard, 1998: A baseline climatology of sounding-derived supercell and tornado forecast parameters. *Wea. Forecasting*, **13**, 1148–1164, https://doi.org/10.1175/1520-0434(1998)013<1148:ABCOSD>2.0.CO;2.

Schenkel, B. A., R. Edwards, and M. Coniglio, 2020: A climatological analysis of ambient deep-tropospheric vertical shear impacts upon tornadoes in tropical cyclones. *Wea. Forecasting*, **35**, 2033–2059, https://doi.org/10.1175/WAF-D-19-0220.1.

——, M. Coniglio, and R. Edwards, 2021: How does the relationship between ambient deep tropical vertical shear and tropical cyclone tornadoes change between coastal and inland environments? *Wea. Forecasting*, **36**, 539–566, https://doi.org/10.1175/WAF-D-20-0127.1.

Schultz, L. A., and D. J. Cecil, 2009: Tropical cyclone tornadoes, 1950–2007. *Mon. Wea. Rev.*, **137**, 3471–3484, https://doi.org/10.1175/2009MWR2896.1.

Sherburn, K. D., and M. D. Parker, 2014: Climatology and ingredients of significant severe convection in high-shear low-CAPE environments. *Wea. Forecasting*, **29**, 854–877, https://doi.org/10.1175/WAF-D-13-00041.1.

——, ——, J. R. King, and G. M. Lackmann, 2016: Composite environments of severe and nonsevere high-shear, low-CAPE convective events. *Wea. Forecasting*, **31**, 1899–1927, https://doi.org/10.1175/WAF-D-16-0086.1.

Spratt, S. M., D. W. Sharp, P. Welsh, A. Sandrik, F. Alsheimer, and C. Paxton, 1997: A WSR-88D assessment of tropical cyclone outer rainband tornadoes. *Wea. Forecasting*, **12**, 479–501, https://doi.org/10.1175/1520-0434(1997)012<0479:AWAOTC>2.0.CO;2.

Stensrud, D. J., J. V. Cortinas Jr., and H. E. Brooks, 1997: Discriminating between tornadic and nontornadic thunderstorms using mesoscale model output. *Wea. Forecasting*, **12**, 613–632, https://doi.org/10.1175/1520-0434(1997)012<0613:DBTANT>2.0.CO;2.

Thompson, R. L., R. Edwards, J. A. Hart, K. L. Elmore, and P. Markowski, 2003: Close proximity soundings within supercell environments obtained from the Rapid Update Cycle. *Wea. Forecasting*, **18**, 1243–1261, https://doi.org/10.1175/1520-0434(2003)018<1243:CPSWSE>2.0.CO;2.

——, C. M. Mead, and R. Edwards, 2007: Effective storm-relative helicity and bulk shear in supercell thunderstorm environments. *Wea. Forecasting*, **22**, 102–115, https://doi.org/10.1175/WAF969.1.

——, B. T. Smith, J. S. Grams, A. R. Dean, and C. Broyles, 2012: Convective modes for significant severe thunderstorms in the contiguous United States. Part II: Supercell and QLCS

tornado environments. *Wea. Forecasting*, **27**, 1136–1154, https://doi.org/10.1175/WAF-D-11-00116.1.

Verbout, S. M., D. M. Schultz, L. M. Leslie, H. E. Brooks, D. J. Karoly, and K. L. Elmore, 2007: Tornado outbreaks associated with landfalling hurricanes in the North Atlantic Basin. *Meteor. Atmos. Phys.*, **97**, 255–271, https://doi.org/10.1007/s00703-006-0256-x.

Virtanen, P., and Coauthors, 2020: SciPy 1.0: Fundamental algorithms for scientific computing in Python. *Nat. Methods*, **17**, 261–272, https://doi.org/10.1038/s41592-019-0686-2.

WSEC, 2006: A recommendation for an enhanced Fujita scale (EF-scale). Wind Science and Engineering Center Rep., 95 pp., https://www.spc.noaa.gov/faq/tornado/ef-ttu.pdf.